SITE CHARACTERIZATION REPORT
SZEK: Zermatt (VS), Kirche

Paolo Bergamo, Manuel Hobiger, Dario Chieppa, Donat Fäh

Last modificaction: 20.03.2018

Schweizerischer Erdbebendienst (SED)
Service Sismologique Suisse
Servizio Sismologico Svizzero
Servizi da Terratrembels Svizzer

ETH Zurich
Sonnegstrasse 5
8092 Zuerich
Schweiz
paolo.bergamo@sed.ethz.ch

Contents

Summary

The SSMNet station SZEK was installed in a small park close to the Pfarrkirche St. Mauritius, in the centre of the municipality of Zermatt (upper Mattertal valley). Active and passive seismic measurements were performed to characterize the subsurface structure beneath the station. The site is characterized by a relatively high fundamental frequency (3 Hz). Performed analyses suggest that site SZEK is probably in a condition of transition between 1D and 2D resonance. In fact, a clear polarization along the valley axis at 2.5 – 3.5 Hz was observed; nevertheless, the resonance peaks show a slight spatial variability which can be related to a sloping interface between the sedimentary formation (debris flow sediments) and the bedrock.

Another site amplification effect related to the geo-morphology of the site is the presence of edge-generated surface waves, as indicated by the appearance of the empirical amplification function estimated for SZEK from regional seismicity.

The subsurface structure beneath SZEK is rather complex, with layers of increasing stiffness at shallow depths (< 23 m, from V_S = 190 to 890 m/s); these overlie a softer formation, which in turn rests on a more compact transition layer, until the bedrock is met (at approx. 49 m depth).

The estimated V_{S30} value for the shallower subsurface is 414 m/s, which classifies the soil as type B according to Eurocode 8 (CEN, 2004), and as type C following SIA261 (SIA, 2014).

1.   Introduction.

In the framework of the second phase of the SSMNet (Swiss Strong Motion Network) renewal project, a new station, labelled as SZEK, was installed on June 2nd 2016 in a small park near the Pfarrkirche St. Mauritius, in the centre of the municipality of Zermatt (Figure 1a). The town of Zermatt is located in the upper Mattertal valley, where its width is of few hundred meters; the centre of Zermatt rests mostly on quaternary formations, of various origins, overlying the valley bedrock (ophiolite). The characterization of the site was ensured by a passive array measurement (outer diameter 244 m) and an active seismic survey (recording line 42 m long), both approximately centred on the location of SZEK.

2.   Geological setting

The centre of Zermatt rests mostly on quaternary formations (moraines, alluvial sediments, debris flow deposits) occupying the bottom of the Mattertal valley, which is locally oriented along a NNE-SSW axis. Station SZEK, in particular, is located on sediments deriving from debris flow.
The quaternary formations overlie the valley bedrock, constituted by ophiolite, which also surfaces in rock outcrops located east, west and south of the town centre (Figure 1b). Available geological information, derived from boreholes drilled in the area (Géoportal du Canton Valais, 2017), indicate that the depth to the bedrock increases from 0 or few to 45 – 50 meters as one proceeds towards the centre of the valley and towards NNE (Figure 1b).
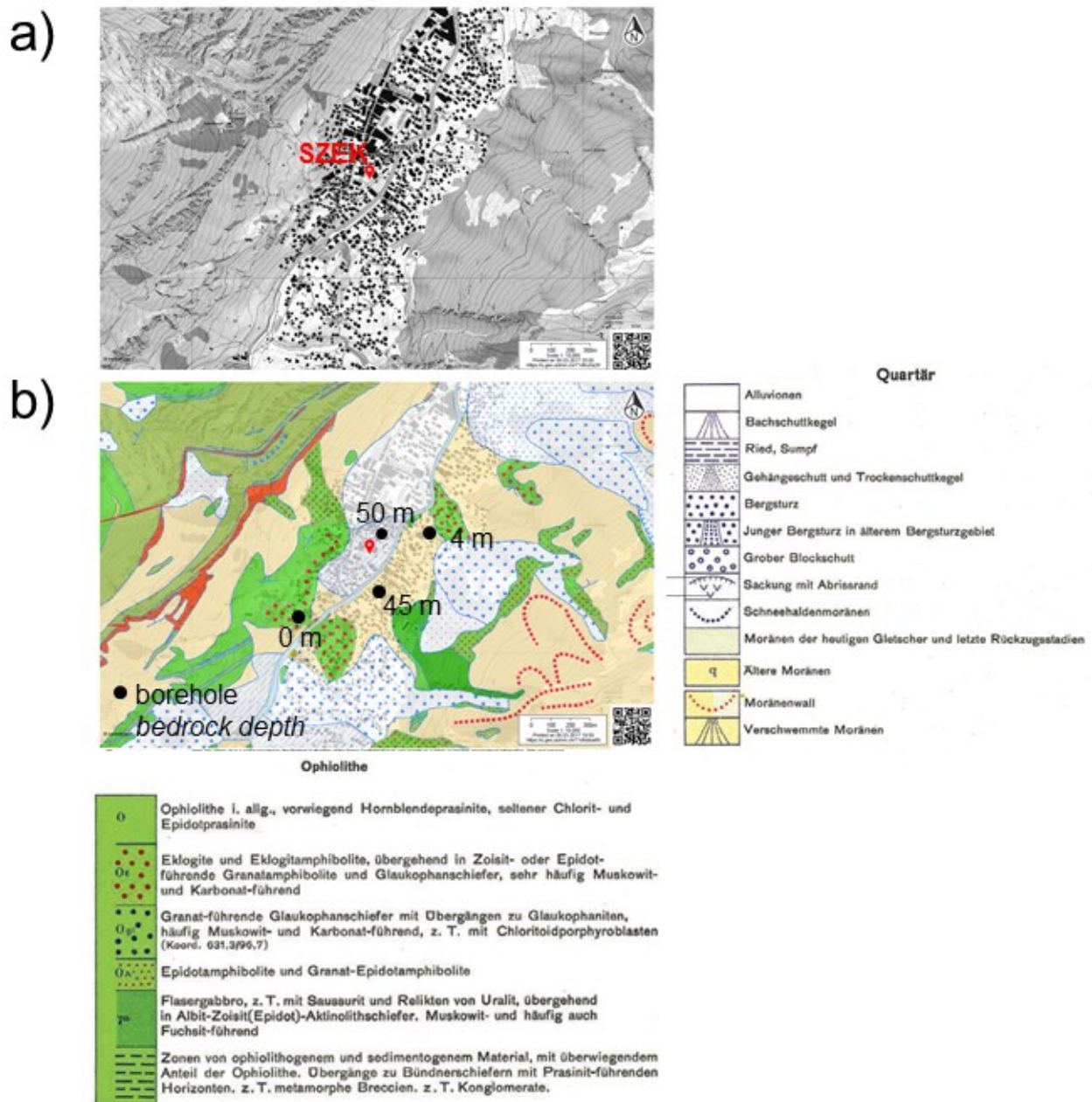
Figure 1 – a) position of SZEK in the centre of Zermatt, and b) on the Swisstopo Geological Atlas. (© 2017 Swisstopo, JD100042). Black dots indicate the position of the closest boreholes, with the labels indicating the bedrock depths.

3.   Seismic acquisition

3.1 Passive seismic acquisition

An array of passive stations was deployed around SZEK in daytime on 9th November 2016; the overall recording time was 155 minutes. The aim was extracting information regarding the propagation at low frequencies (< 10 Hz) of surface waves generated by either human activities or natural sources.

3.1.1 Equipment and geometry of the acquisition array

The ambient seismic recordings were performed using ten Lennartz 3C 5s seismometers connected to Centaur dataloggers; the sampling frequency was set to 200 Hz. The sensors were all placed on metal tripods, the soil surface ranged from natural soil to cobblestone or asphalt (Figure 2a). The array layout was planned to consist of three concentric rings (radii of 36, 60 and 135 m), with three stations each, around a central station. Due to local constraints, the final array configuration differed from this theoretical layout, especially the central station of the array was not in the center of the three rings. The inter-station distances of the final array range from 25.7 to 244.4 m. The station names of the different stations all consist of 'SZEK' followed by two digits according to the serial number of the Centaur used (i.e. 42 – 46, 48, 49 and 53 – 55). The locations of the different sensors are indicated in Fig. 3.

The locations of the different sensors have been measured using a differential GPS system (Leica Viva GS10) which was set up to measure with a precision better than 5 cm. For most stations, this precision was obtained. For SZEK46, the position was measured with a precision of 8.7 cm, for SZEK49 with 12.7 cm, and for SZEK48, no better precision than 2.24 m was obtained. Because SZEK48 and SZEK49 were both located on the outermost ring, this measurement error mostly affects the very low frequency end of the measurement.
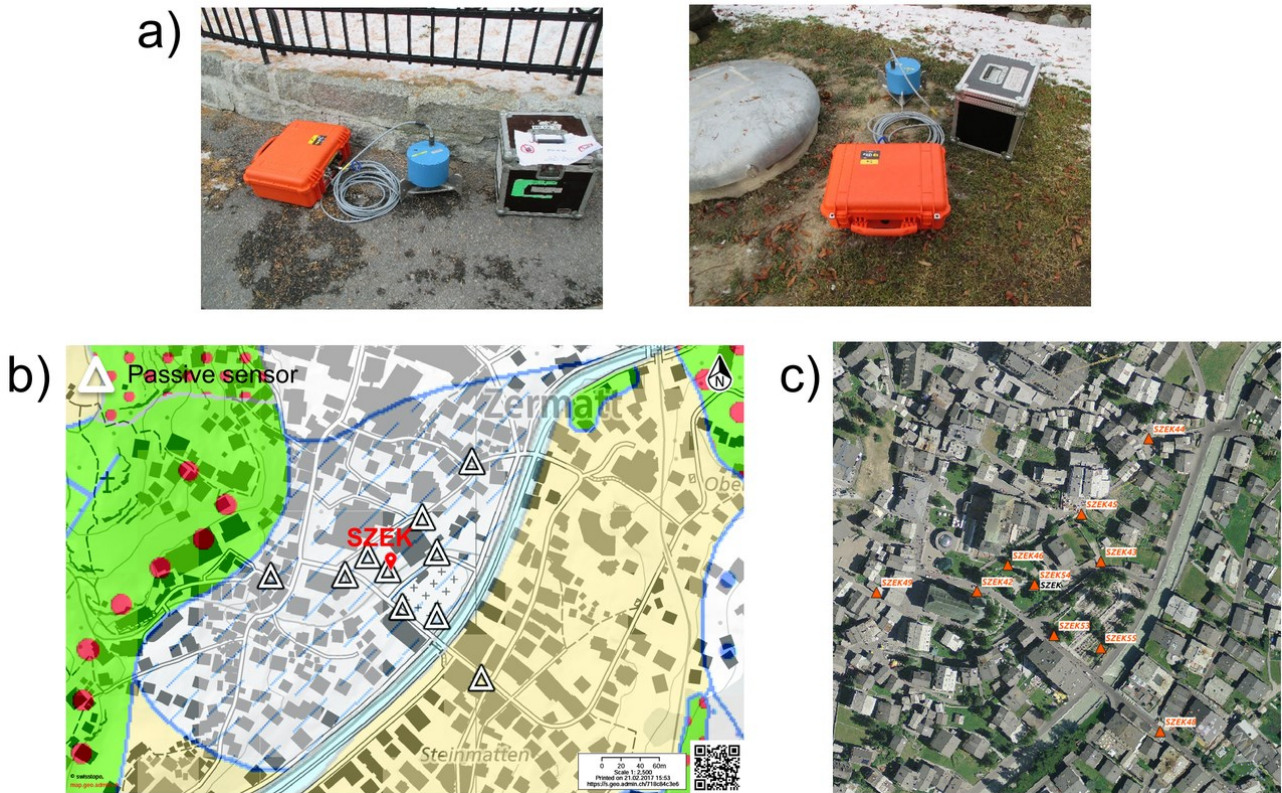
Figure 2 – a) Lennartz sensors put in place (in the right hand side picture the vault of the permanent station SZEK is visible). b) Geometry of the acquisition array (sensors are represented as triangles) superimposed on the Swisstopo Geological Atlas. (© 2017 Swisstopo, JD100042). c) Aerial image of the passive array in Zermatt: the stations of the passive array are indicated by orange triangles.

3.2 Active survey

To ensure investigation coverage also for higher frequencies (> 10 Hz), and to investigate in detail the shallow near-surface at the location of station SZEK, an active survey was conducted in parallel with the passive recording. For the sake of a comprehensive subsurface characterization, multichannel analysis of surface waves (MASW; Park et al., 1999) and P-wave refraction (Redpath, 1973) acquisitions were conducted.

3.2.1 Equipment and geometry of the acquisition array

We used two sets of 8 three-component geophones, having a corner frequency of 4.5 Hz. Each set of sensors was connected to a Geode data logger; the two Geodes were coupled for time synchronization (Figure 3a). As a seismic source, a 5-kg sledgehammer hitting a flat metal plate was used; the synchronization between the recordings and the shooting source was ensured by a trigger device fastened to the hammer handle.

The receivers were deployed along a straight line lying across the small green area where SZEK is located (Figure 3b). Geophones were mostly coupled to the ground thanks to metal spikes penetrating the soil; two of them fell on stone paths, hence they were simply placed on the rock slabs. The inter-geophone distance was 2.8 m, leading to an array length of 42 m. The source was operated at four

different locations, at both ends and at two intermediate positions of the geophone spread (src1-4 in Figure 3b). All acquired seismograms were exploited for P-wave refraction analyses; traces recorded with the source placed at src1 and src2 were used for surface wave analysis.
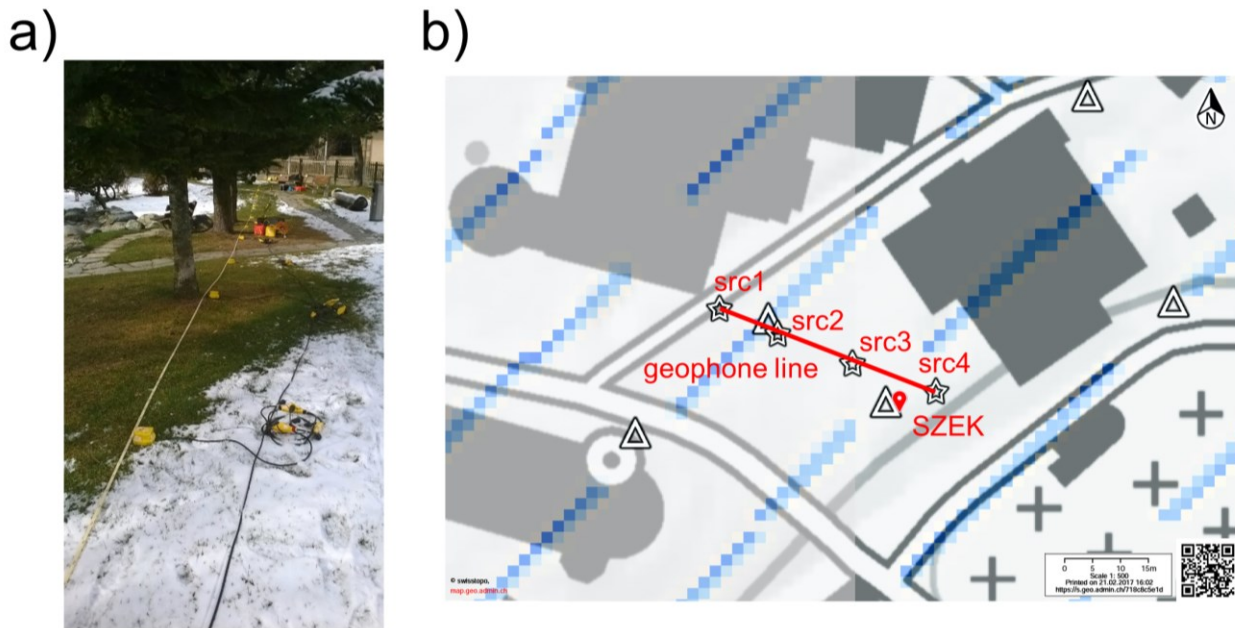

Figure 3 – Active seismic array. a) Active array in place; b) Map of the array: the geophone line is represented with a red line, the shooting positions as stars labelled as src1 to src4.

3.2.2 Acquisition

The time-sampling parameters adopted for both MASW and refraction acquisitions were the following: sampling interval = 62.5 µs, record length = 1 s, pre-trigger delay = -0.05 s.

In order to ensure a good spatial sampling, particularly for refraction data, given the limited number of available geophones (16), these were successively arranged in two configurations:

- configuration 1: the 16 geophones are evenly spaced by 2.8 m along a line connecting src1 (where receiver 1 is located) to scr4 (where receiver 16 is located).
- configuration 2: geophones 1-15 are shifted towards SE (i.e. towards src4) by 1.4 m. In this case, the traces recorded by geophone 16 (left in the same position of configuration 1, i.e. at src4) are discarded because redundant.

With both configurations, the hammer blow was repeated 10 times at each shooting point (src1 – src4); for each shot, the recordings from all geophones were saved in a separate *.sg2* file. Combining the traces from both array configurations, we obtain a "virtual" seismic line of 31 three-component receivers, evenly spaced by 1.4 m along a 42 m long line.

As example, in Figure 4 we show the seismograms (vertical component) acquired with both recording configurations, the source being located at src1.
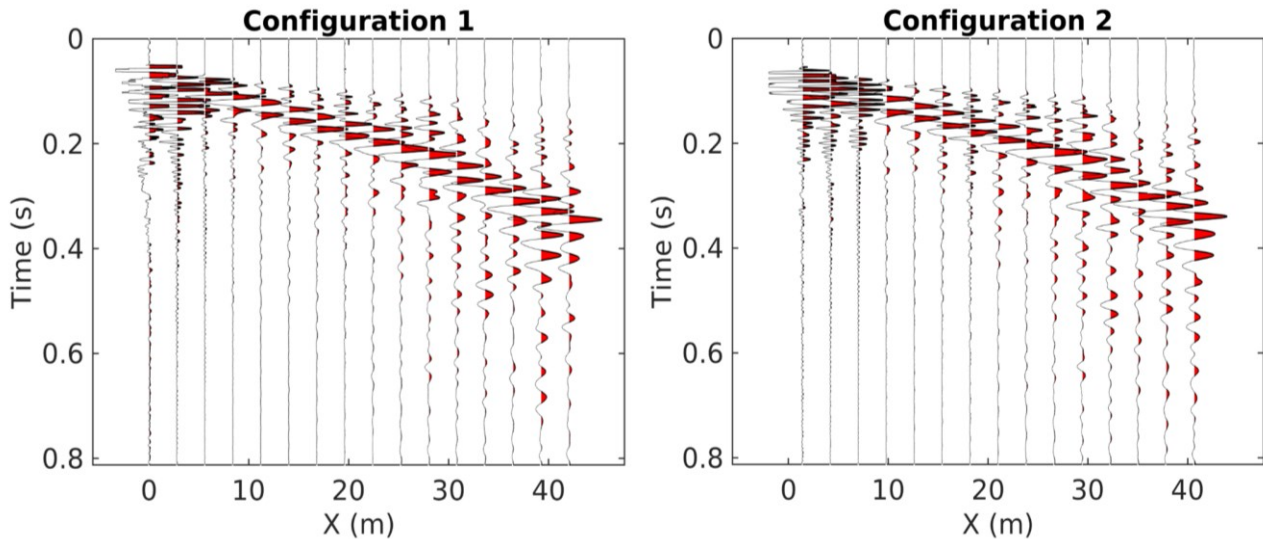
Figure 4 – Seismic traces (vertical component) acquired with the source positioned at src1. The left panel represents the recordings from the geophones in configuration 1 (receivers placed at X=0:2.8:42 m); in the right panel, the traces from configuration 2 (receivers 1-15 shifted by 1.4 m towards the end of the line). The X coordinate reference system has its origin at src1 (X =0 m) and progresses towards src4 (X = 42 m).

4. Data processing

Data acquired in the active and passive surveys were processed in order to determine the characteristics of propagation of surface waves (passive array acquisition) and surface and P-waves (active acquisitions).

4.1 Passive data processing

4.1.1 H/V analysis

The seismic data (three component traces) acquired by each sensor of the passive array were processed with:

-        classical H/V techniques (as implemented in Geopsy software, www. geopsy.org; classical H/V of Fäh et al., 2001), determining the spectral ratio between horizontal and vertical components (Nakamura, 1989), whose peaks are related to the frequencies of resonance of the site;

-        more refined algorithms, estimating the ellipticity of Rayleigh wave as a function of frequency (Raydec, Hobiger at al., 2009; time-frequency method, Poggi and Fäh, 2010; wavelet-based time-frequency method as implemented in Geopsy software). These methods aim at eliminating the contributions of other waves besides Rayleigh waves, to obtain a more reliable estimation of Rayleigh wave ellipticity when compared to the classical H/V technique.

As an example, Figure 5a represents and compares the H/V curves obtained applying different methods for SZEK54, the sensor placed next to the station SZEK (see Figure 2a, right panel). All techniques agree in identifying a first peak centered around 3 Hz, followed by a trough at approx. 5 Hz and a second peak at 10 Hz. The first two features (first pronounced peak at 3 − 4 Hz, followed

by a marked trough) can also be identified in the H/V curves from all the passive array sensors; the second peak in the $5 - 20$ Hz frequency band is clearly present only in a few more curves, as most of them show H/V values below 1 in that interval (Figures 5b, 6).
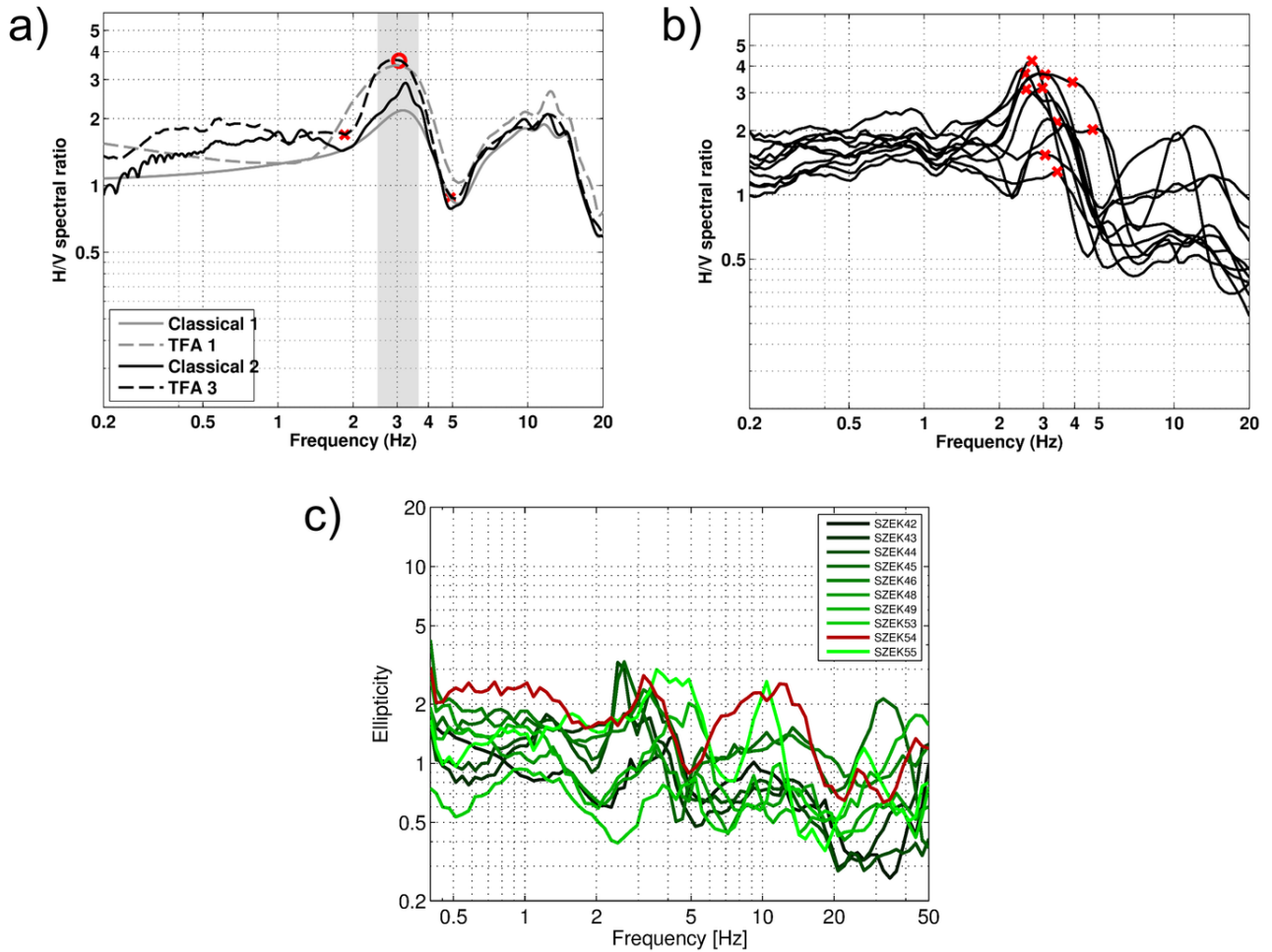

Figure 5 – H/V ratio and ellipticity analyses. a) comparison among different methods for the estimation of H/V ratio and ellipticity for SZEK54, the sensor located closest to SZEK (Classical 1: Fäh et al., 2001; TFA1: Geopsy wavelet-based time-frequency method; Classical 2: Geopsy classical H/V; TFA3: Poggi and Fäh, 2010). b) H/V curves (method: TFA3) from all the sensors of the passive array: red crosses mark the identified f_0. c) ellipticity curves obtained with the application of the RayDec technique (Hobiger et al., 2009); the sensor closest to SZEK (SZEK54) is represented with a red line.
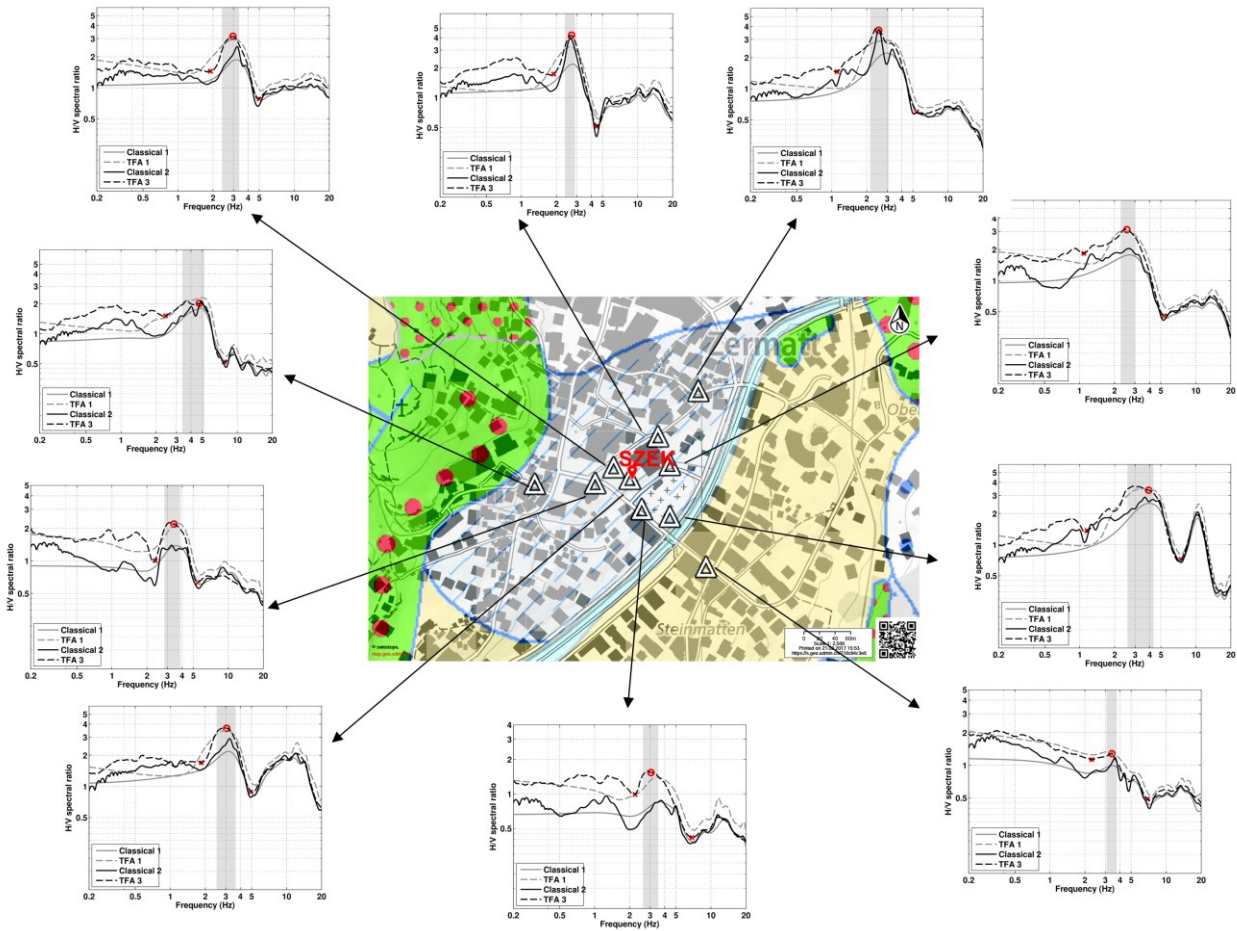
Figure 6 – H/V analysis. The insets surrounding the map of the passive array contain the H/V curves for each location (graphs are similar to Figure 5a).

The fundamental frequencies (f_0) were picked for all stations of the passive array, using the curve obtained with the time-frequency method of Poggi and Fäh (2010) as reference graph (red crosses in Figure 5b, red dots in Figure 6). The spatial distribution of picked frequencies is represented in Figure 7.
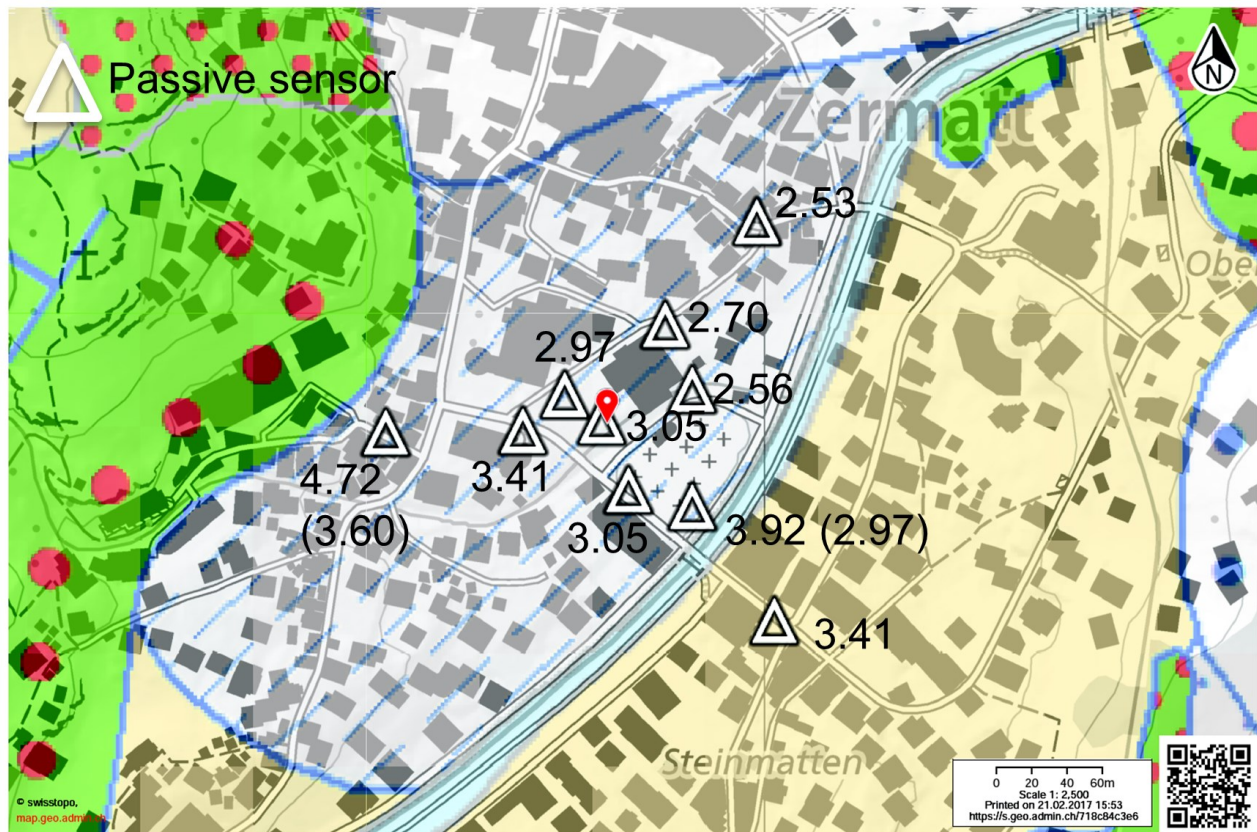
Figure 7– Spatial distribution of identified f_0, in Hz. A second value has been added between brackets for those sensors whose corresponding H/V curves present a relative maximum in the 2.5 – 3.6 frequency band, beside the absolute maximum reported outside brackets.

As evident in Figures 5b and 6, all the identified fundamental frequencies lie within the range 2.5 – 3.6 Hz, with the exception of two outliers (3.92 and 4.72). However, in these two cases, the H/V curves present broad peaks, with additional relative maxima in said frequency interval (see Figures 5b, 6). Therefore, these maxima were picked as well, and they are reported in brackets in Figure 7.

The results of the polarization analysis, performed on the same passive recordings, seem to suggest that the peaks at 2.5 – 3.6 Hz are related to a 2D resonance of the site (see following section). Nevertheless, these peaks present a spatial variability, while strictly speaking the frequency of 2D resonance of a sedimentary basin should be spatially invariant (Bard and Bouchon, 1985). In fact, along the direction transversal to the valley axis (WNW – ESE), frequency values decrease with the distance from the valley shoulders; along the valley axis (SSW – NNE), f_0 decreases following the valley gradient; in a 1D resonance interpretation, this trend would indicate a sediment-bedrock interface deepening at the centre of the valley and towards NNE.

The coexistence of 1D and 2D resonance effects could be explained with an intermediate condition between these two states: this hypothesis is discussed in section 6.2.

4.1.2 Polarization analysis

Considering the geomorphology of the site, a polarization analysis on the array data was performed to check for 2D resonances using the method of Burjánek et al. (2010): the results are represented in Figures 8 and 9.

Consistently with the H/V analysis presented in the previous paragraph, we observe marked troughs in the ellipticity graphs in the 2.5 – 3.5 Hz frequency range (Figure 8). We remind that, according to Burjánek et al. (2010) the ellipticity is here (Figure 8) defined as the ratio between the semi-minor and semi-major axes of the ellipse that describes the particle motion in the 3D Euclidean space for each considered time window and frequency; therefore, the particle motion related to the propagation of Rayleigh waves is indeed characterized by low values of ellipticity, for the frequencies with prevalent horizontal motion (for which we have a peak in the H/V curves of Figure 6).

As far as the strike is concerned, in said frequency band (2.5 – 3.5 Hz), the preferential direction is SSW – NNE (Figure 9), which coincides with the orientation of the valley axis. Only two sensors deviate from this trend; the first one is SZEK55, located in the south-eastern portion of the array and the closest to the Matter Vispa river crossing Zermatt, therefore probably "disturbed" by the noise produced by the river. The second sensor is SZEK48, marking the southeastern corner of the passive array; this is the only station located on the moraine deposits occupying the right bank of the Mattertal (all other sensors were deployed in the north-western part of the valley floor, covered by debris flow sediments: see Figures 2).

The consistent orientation of strikes in Figure 9 may suggest the existence of 2D resonance phenomena for the investigated site, related to its geomorphology; however, this feature is not in agreement with the observed spatial variability of the fundamental frequency peaks (see previous paragraph). See section 6.2 for a full discussion of this aspect.
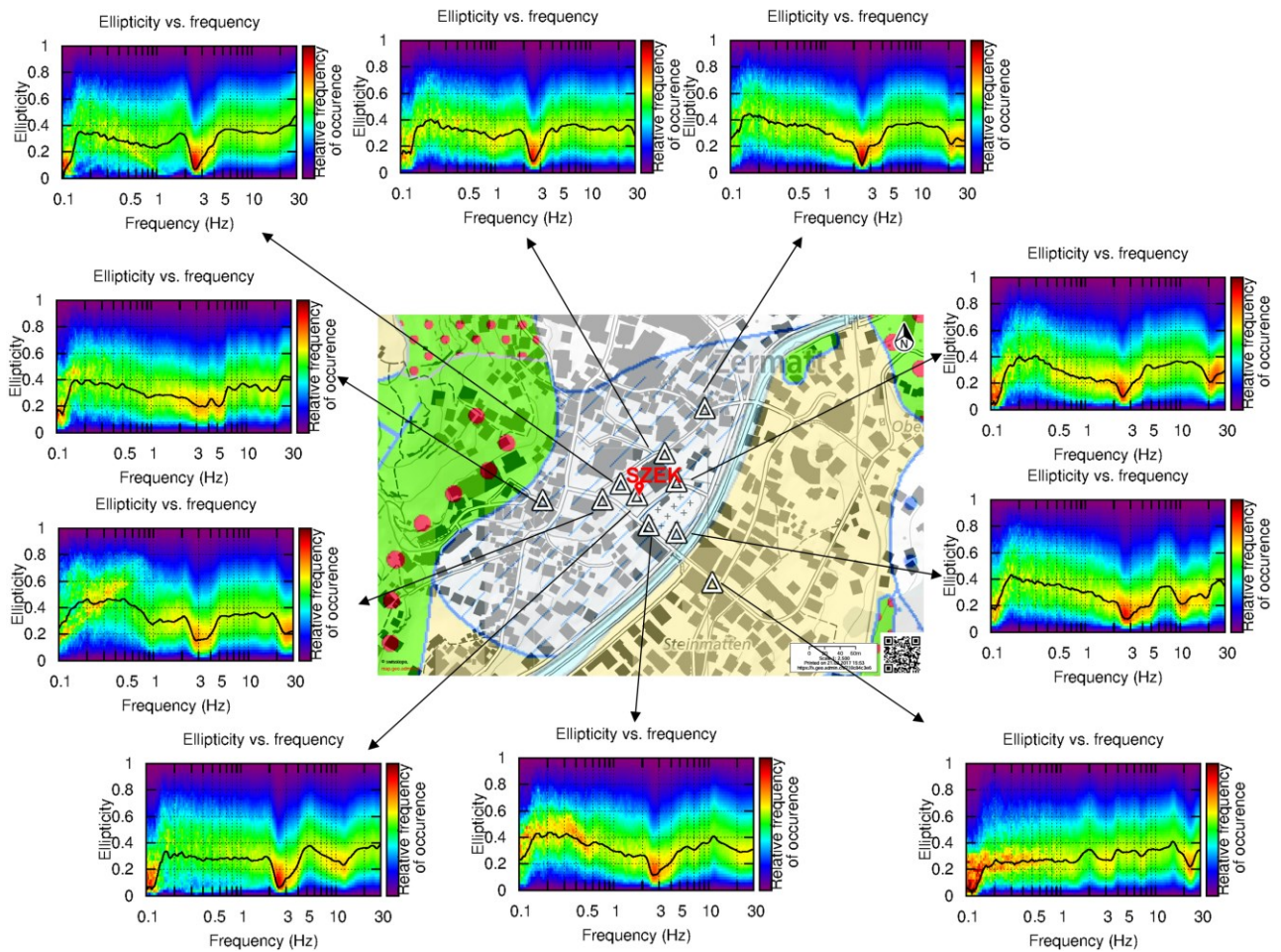
Figure 8 – Polarization analysis. The insets surrounding the map of the passive array contain the ellipticity (as defined in Burjánek et al., 2010) graph for each sensor (a trough in the ellipticity corresponds to polarized motion).
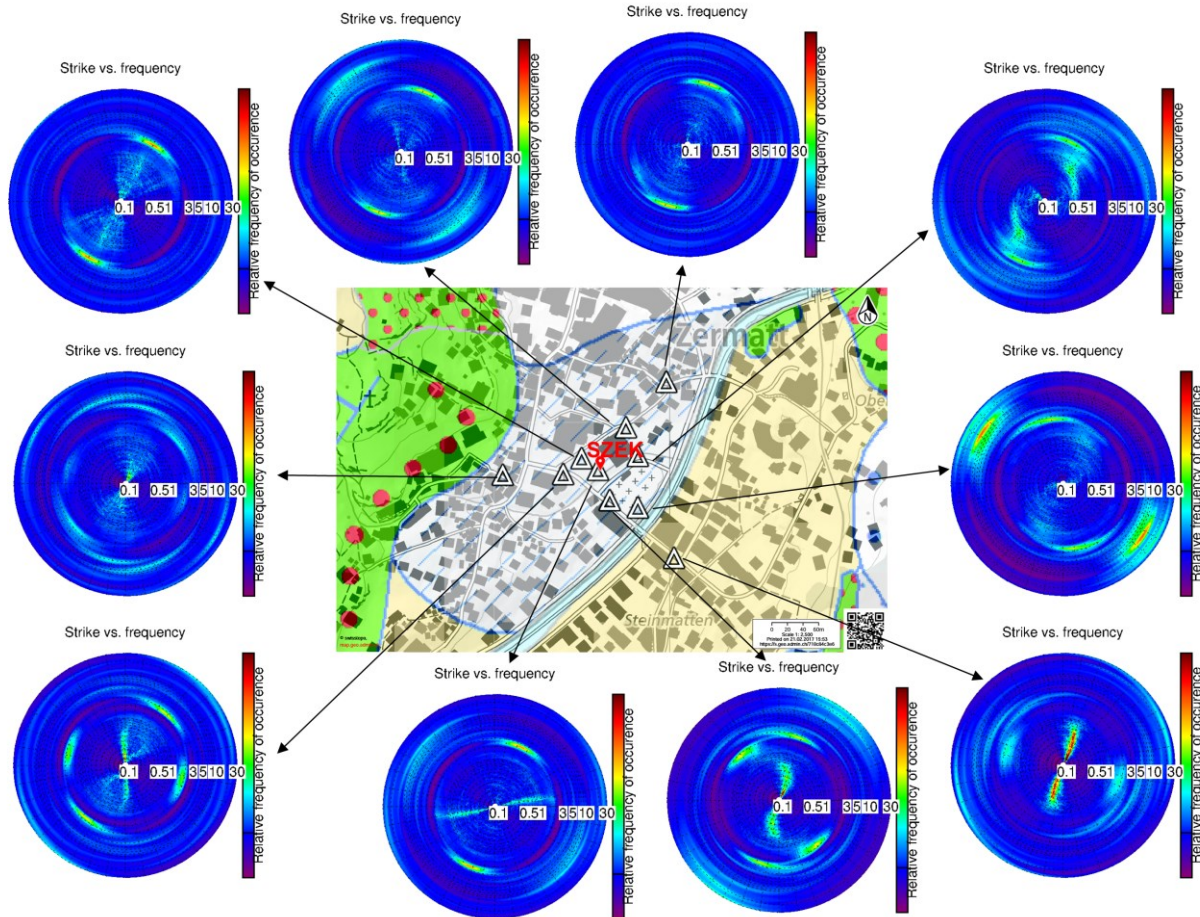
Figure 9 – Polarization analysis. The insets surrounding the map of the passive array contain the polarization strike graph for each sensor.

4.1.3 Three-component high-resolution fk

Besides single-station interpretation, the recordings from the passive array were also collectively processed, with the aim of estimating the parameters of propagation (phase velocity, ellipticity, azimuth) of surface (Rayleigh and Love) waves. The used technique is the three-component high resolution *fk* analysis of Poggi and Fäh, 2010. Results are shown in Figures 10 and 11. A Rayleigh wave dispersion curve, interpreted as the fundamental mode, can be recognized (and was therefore picked) in the vertical component phase velocity graph, between 4 and 11 Hz (top left panel in Figure 10). The dispersion image is less clear in the radial component panel (top centre); consequently, the ellipticity curve (bottom left panel), portraying the ratio between corresponding horizontal and vertical components of Rayleigh waves, cannot be considered as reliable. Finally, a well-defined dispersion curve, stretching between 3 and 11 Hz, is evident in the transverse component panel, which refers to the propagation of Love waves (top right); again, it was interpreted as fundamental mode. Considering the geomorphology of the site, prone to preferential directions of propagation, the distribution of the azimuths of the waves identified as Rayleigh and Love wave fundamental modes was also analyzed. Figure 11 shows that both Rayleigh (top panel) and Love waves (bottom panel), travel mostly with an azimuth of around 45° or 225° (more markedly), approximately in the whole

15

considered frequency range; this direction coincides with the axis of the valley (SW-NE). These results are not surprising, as the valley hosts the majority of human activities which produce the identified surface waves.

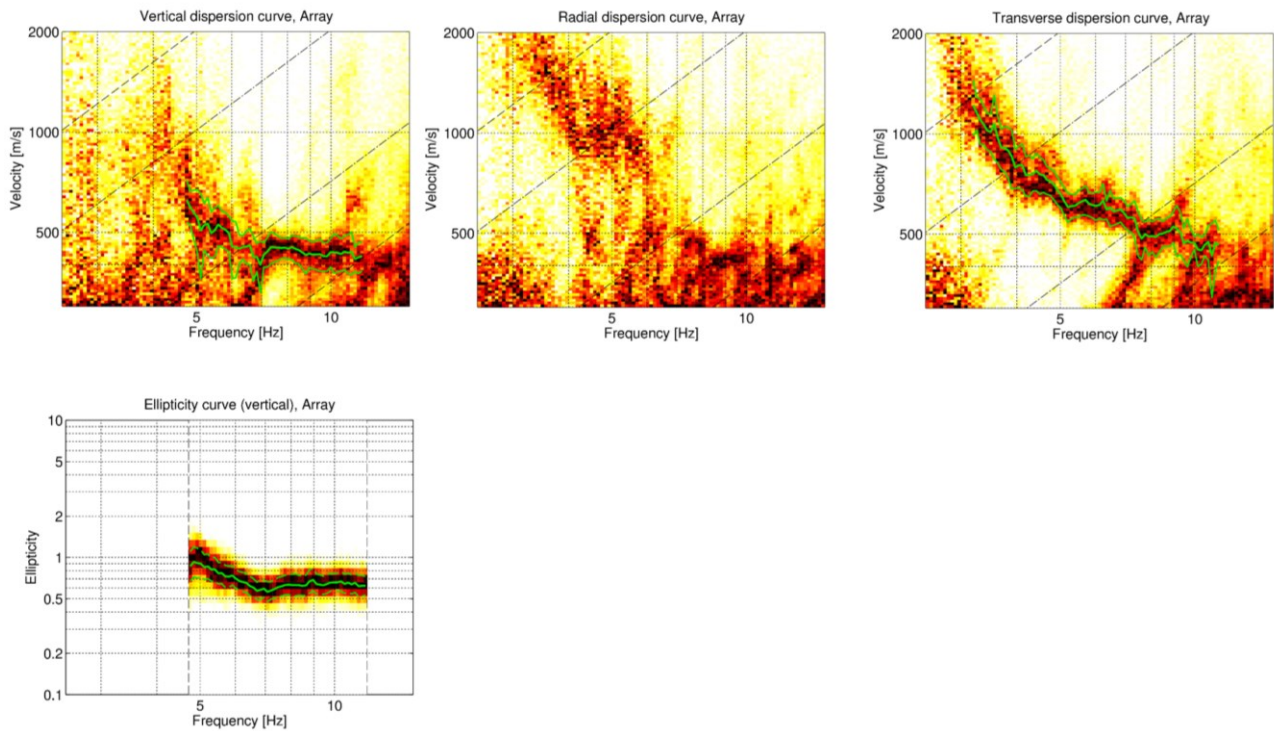*Figure 10 – Three-component high-resolution fk processing results. Top row: phase velocity vs frequency graphs obtained from vertical component (left), radial component (centre), transverse component (right). Bottom row: ellipticity curve. Dashed lines indicate the array resolution limits, while green lines indicate the picked dispersion curves (central values and standard deviation interval).*
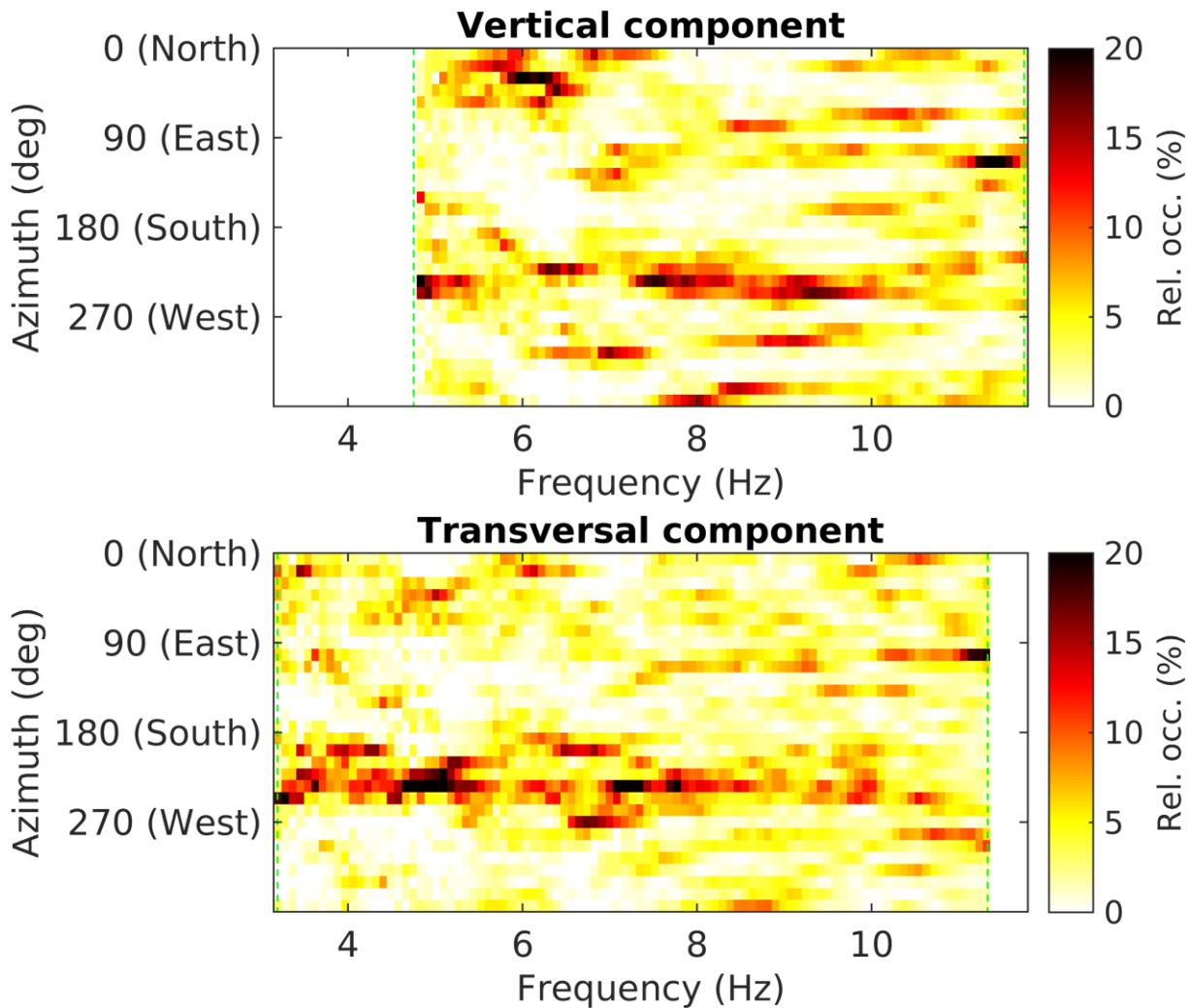
Figure 11 – Three-component high-resolution fk results. Relative occurrence of azimuth values, as a function of frequency, for the waves appearing in the vertical (top) and transversal (bottom) component recordings. The azimuth angle is 0 for North direction and it increases clockwise. Only the data within the picking areas (upper and lower green lines) of Figure 10 (top left and right panels) were considered for the representation.

4.2 Active data processing

4.2.1 P-wave refraction

Seismic traces generated by different shots, with the seismic source at the same location (10 shots for each configuration), were summed – or stacked – in time domain. This was done to enhance the coherent seismic events generated by the controlled seismic source, and at the same time to minimize the incoherent noise present in the recordings (Foti et al., 2015). "Stacked" seismic sections, with greater signal-to-noise ratio, were hence obtained. To preserve the effectiveness of the stacking operation, the vertical components of the seismic traces at short offsets were cross-correlated to ensure a robust synchronization among the seismograms.

P-wave first-break arrival times were manually picked on all the available vertical component stacked seismograms. Figure 12a represents two sample seismic sections and the identified first-breaks; the complete set of obtained travel-time curves (one for each considered shooting position) is shown in Figure 13b. Comparing the two sections of Figure 12a, it is clear that P-wave travel time curves are not symmetrical, indicating the presence of lateral variations along the active seismic line. Observing the whole set of hodocrones (Figure 12b), these assume two different appearances (aligning along either a two- or three-segment line), depending whether both source and receiver are located before or past $X \approx 25$ m. The two groups of travel times were interpreted separately (Figure 13a) with the intercept time method (Reynolds, 2011) yielding a three-layer model for the subsurface portion $X <$ 25 m, and a two-layer model for the portion at $X > 25$ m (Fig 13b).

A possible explanation for this variation can be provided by the configuration of the site where the seismic line was deployed. As earlier anticipated, station SZEK and the active array are located in a small, rectangular park in the centre of Zermatt (Figure 3); the soil surface degrades gently towards east (Figure 13c), until a steep slope, 4 m high, is met at the eastern border of the park. Therefore, it is possible to suppose that the three-layer system below the western portion of the spread is composed of artificial soil cover of the park (V_P = 340 m/s), overlying an intermediate layer (540 m/s) and finally a stiffer formation of sand, gravel and pebbles (1040 m/s, i.e. the debris flow sediments indicated by the geological map, Figure 1). The eastern end of the active array ($X > 25$ m) rests on an artificial embankment put in place to level the surface of the park, and made up of the same material (V_P = 315 m/s) of the soil cover of the $X < 25$ m model; this artificial fill rests directly on the sand, gravel and pebbles layer (V_P = 950 m/s). It should be noted that most probably station SZEK was installed on this artificial embankment (see Figure 3b).
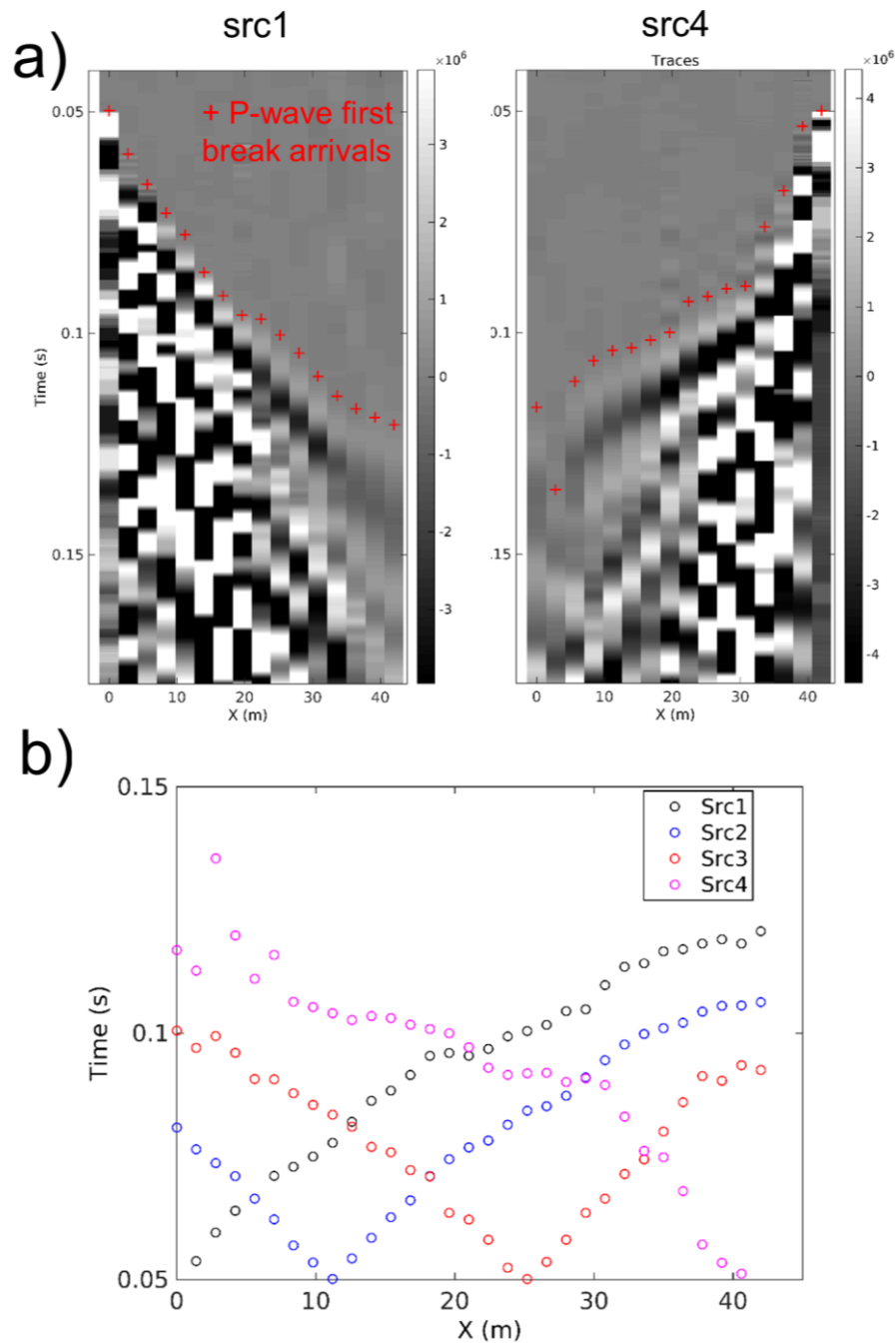
Figure 12 – P-wave refraction processing. a) Example of picking of first-break P-wave arrivals, on two stacked seismic sections with the source positioned in src1 and src4, respectively; b) all collected travel-time curves.
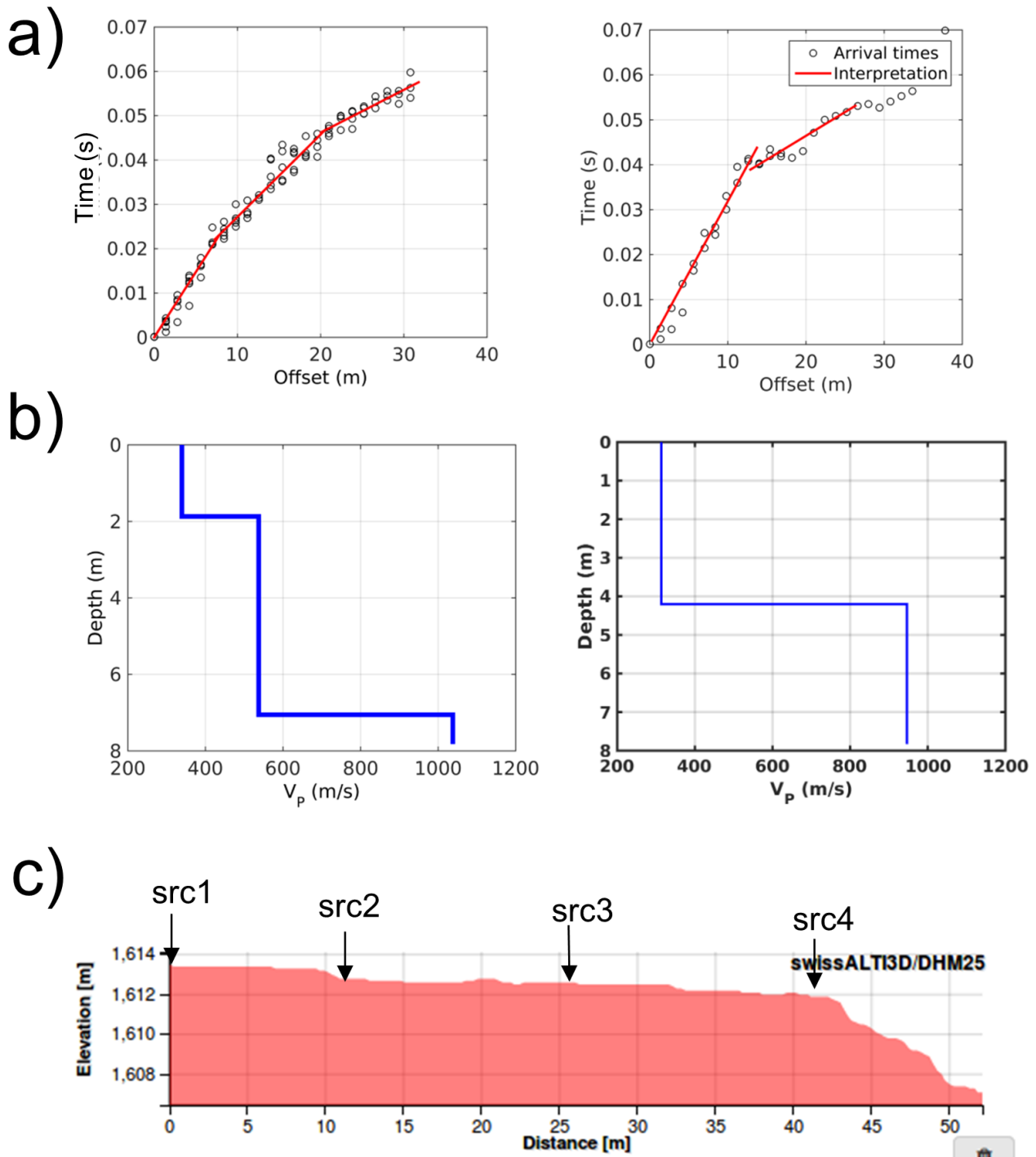
Figure 13 – P-wave travel-time interpretation. a) Intercept time interpretations of the travel time curves from the interval 0 < X < 25 m (left panel) and from 25 < X < 42 m (right panel). b) Derived P-wave velocity profile. c) Topographic profile of the active survey line.

4.2.2   MASW f-k processing

Rayleigh wave dispersion data were extracted from the vertical and longitudinal component seismograms from MASW acquisitions (the source being positioned at both ends of the array, src1 and src4 in Figure 3b; the traces at short offset, < 5 m, were excluded from the processing to mitigate

near-field effects). The considered seismic sections were processed by means of a 2D *f-k* (frequency – wavenumber) transform (Socco and Strobbia, 2004), in order to obtain a conversion of the recorded sets of traces from time-offset to frequency-wavenumber domain. *f-k* panels from single shot records with the same source and receiver positions were summed to obtain spectral images with greater S/N ratio (O'Neill, 2003; Neducza, 2007). Prior to the application of the *f-k* transform, seismic traces were attributed the weights of a Hanning window (Boiero, 2009). The purpose of the windowing operation is twofold: reducing the numerical artifacts of the Fast Fourier Transform, and focusing the analysis on the subsurface portion below the centre of the array (therefore mitigating the effect of lateral variations to retrieve a univocal dispersion image).

The energy maxima corresponding to the Rayleigh wave dispersion curves were picked on these stacked *fk* panels (Socco and Strobbia 2004, Foti et al., 2015). Spectral amplitude peaks from individual shot recordings were identified as well, and used to define the uncertainty intervals in the estimation of phase velocities (Socco et al., 2009; Boiero and Socco, 2010).

Figure 14 shows the stacked *f-k* panels for recording configuration 1 and sources at src1 and src4, as well as the corresponding picked energy maxima; all the obtained Rayleigh wave dispersion curves (from recording configurations 1 and 2) are displayed in Figure 15a. The dominant feature in all *f-k* spectra is an event extending continuously from 10 to 60 Hz, with phase velocities decreasing from 450 to 200 m/s. This branch was identified as fundamental mode. Three additional higher modes (first to third higher) were also recognized in most of the stacked *f-k* panels. Phase velocity data points obtained from different shooting/recording configurations and recording components were then averaged in a single dispersion curve representative for the site (blue dots in Figure 16b); this curve approximately matches the velocities of the Rayleigh wave fundamental mode obtained from the passive array (black dots) in an overlapping frequency band centered at 10 Hz.
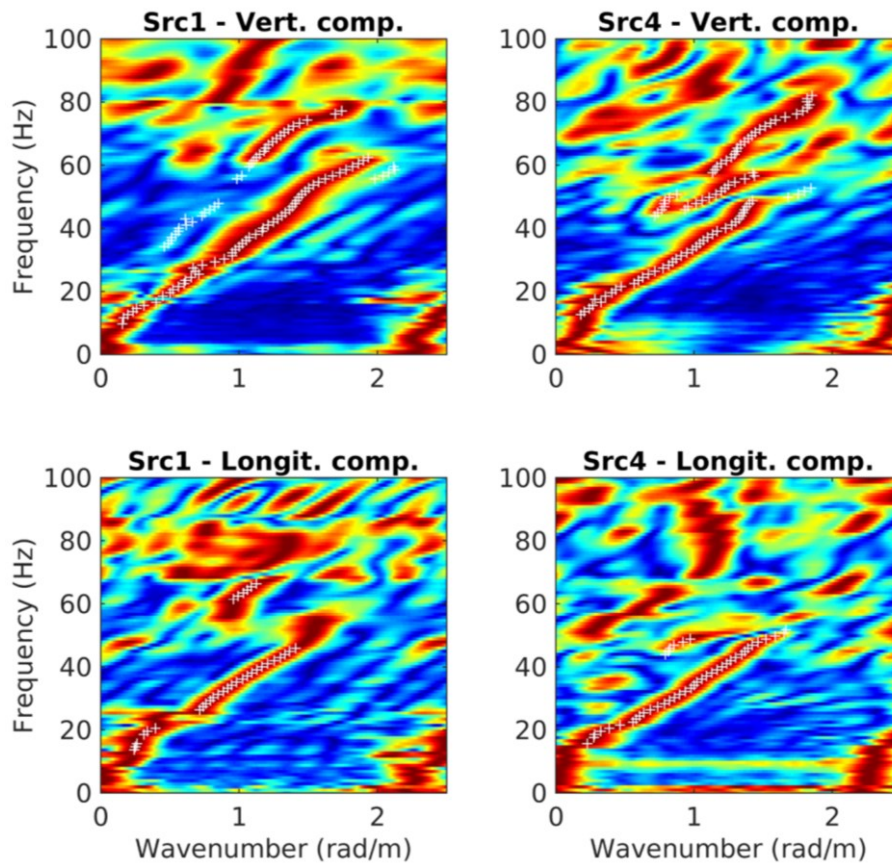
Figure 14 – Stacked, normalized f-k spectra obtained from vertical and longitudinal components of seismic sections acquired with the source positioned in src1 or src4, and the geophones placed in configuration 1 (see section 3.2.2). White dots are the picked energy maxima, corresponding to Rayleigh wave dispersion curves.
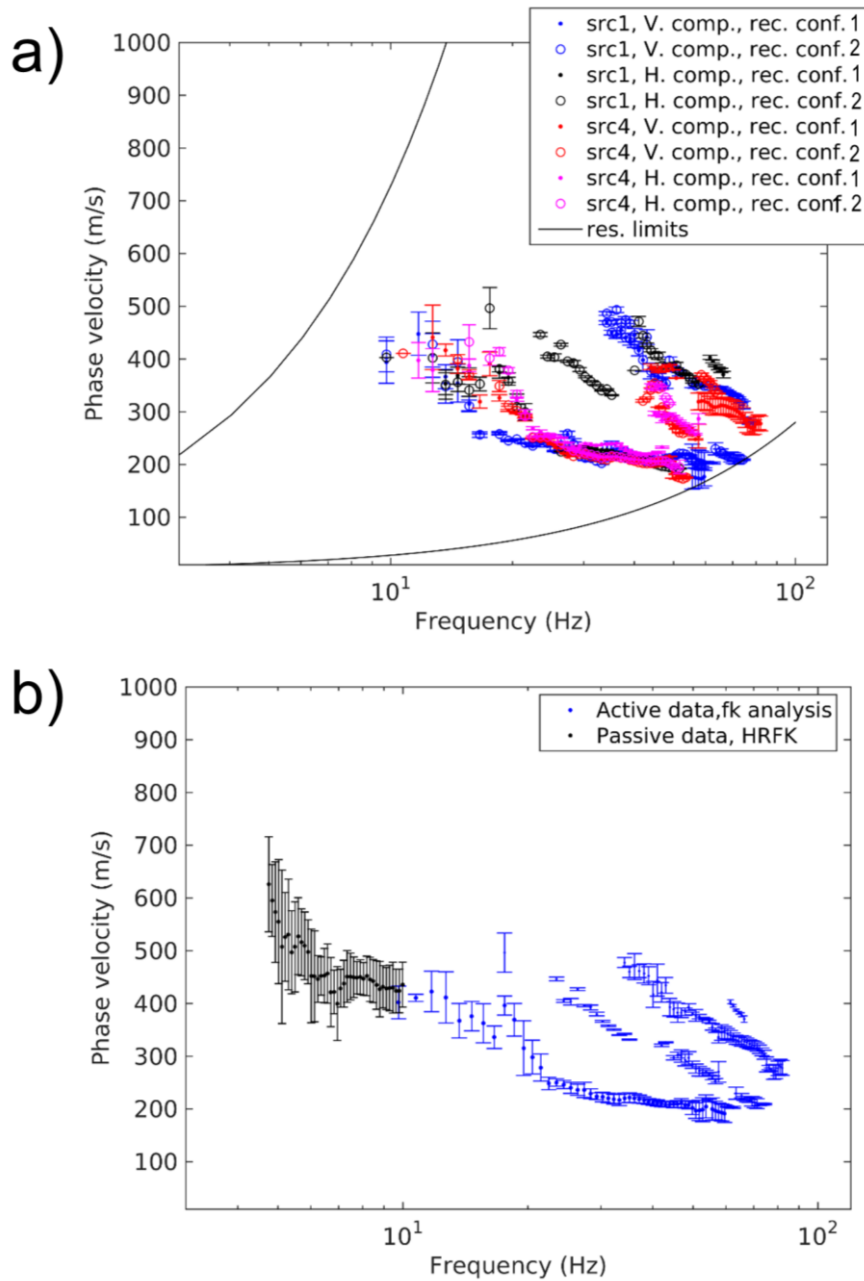
Figure 15 – Extraction of Rayleigh wave dispersion curves from active data with f-k analysis. a) Dispersion curves extracted from stacked f-k panels; b) average dispersion curve (blue dots), collated with the Rayleigh wave fundamental mode from passive data (black dots, see section 4.1.3).

4.2.3   WaveDecActive

Three-component seismic traces acquired with the source positioned in src1 and src4 and receivers in configuration 1 and 2 were also processed with the WaveDecActive code (Maranò et al., 2017), with the aim of retrieving the properties of Rayleigh wave propagation in terms of both phase velocity and ellipticity. WaveDecActive implements a maximum likelihood algorithm for the analysis of Rayleigh waves generated by a controlled source. Differently from the conventional *f-k* analysis approach (see previous section), it is able to characterize the Rayleigh wave propagation both in terms of phase velocity and ellipticity angle. Key parameters required by WaveDecActive are the definition

of the maximum number of Rayleigh waves that the code attempts to identify, and the value of parameter γ, which is able to modify the approach of the code towards wave identification from a Bayesian information criterion (γ = 1) to a maximum likelihood approach (ML, γ = 0), or a compromise between the two (0 < γ < 1). Following the recommendations of the code's author (Maranò, 2016) and some preliminary attempts, the maximum number of waves was set to 5 and γ to 0.1, thus opting for an approach relatively close to a maximum likelihood solution.

The phase velocity estimates obtained from all considered shots are displayed in Figure 16a (red dots); despite the significant presence of outliers, a dispersive event in agreement with the fundamental mode from the *f-k* analysis (black curve) can be recognized. The set of data points selected as Rayleigh wave fundamental mode is shown in Figure 16b; the corresponding values of ellipticity angle are displayed in Figure 16c.
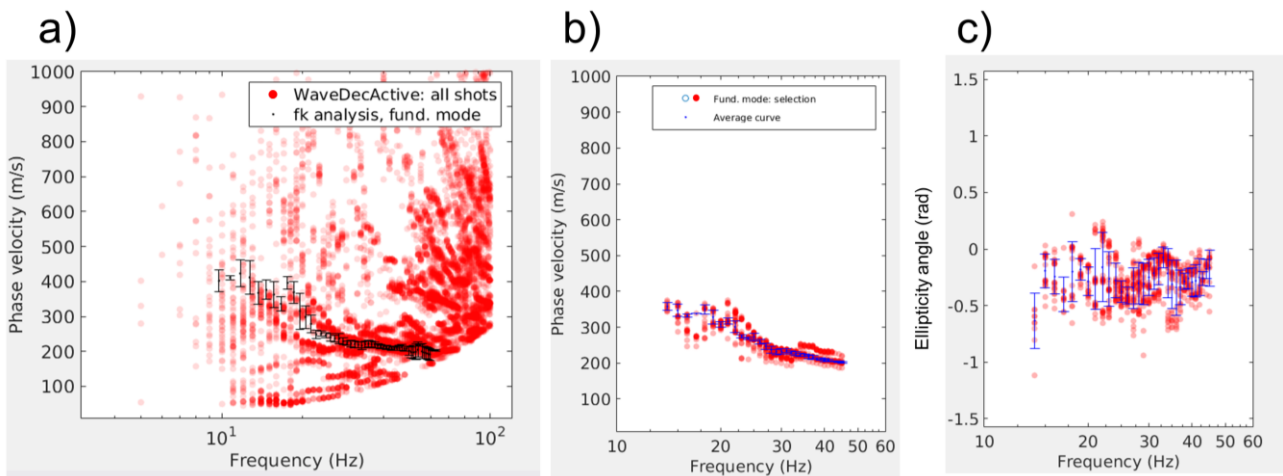

Figure 16 – WaveDec Active processing results. a) Rayleigh wave phase velocity estimates from all considered shots (red dots); the fundamental mode of the curve from the f-k analysis (see previous section) is also superimposed (black dots). b) Selection of data points attributed to the fundamental mode. c) Ellipticity angles for the data identified as fundamental mode.

5   Surface wave data inversion

The retrieved phase velocity dispersion curves of Rayleigh and Love waves (section 4) were inverted for a 1D profile of the seismic properties of the subsurface. The inversion was performed using the Dinver software of the Geopsy suite that implements an Improved Neighborhood Algorithm (Wathelet, 2008).

5.1   Inversion target

As for Rayleigh wave phase velocity data, the multimodal dispersion curve obtained from the *f-k* analysis of active MASW measurements was merged with the fundamental mode branch from the passive array processing (Figure 15b). The fundamental mode of Love waves, as retrieved from the passive data with the high-resolution *f-k* analysis (Figure 10, upper right panel), was also considered for the inversion. Phase velocity uncertainties, as obtained from the processing operations presented in section 4, were taken into account. The possible presence of 2D resonance effects, as discussed in

section 4.1.2, does not allow to include the retrieved ellipticity information in the inversion target (Michel et al., 2014).

The dispersion curves selected as final inversion target are represented in Figure 17. It is worth remarking the fact that around 5 Hz the Love wave phase velocities are higher than the Rayleigh wave fundamental mode. In the practical experience of the author, this feature suggests the presence of a velocity inversion (i.e. a stiffer layer embedded between softer formations) in the V_S profile of the investigated area (see also Bergamo et al., 2016). This indication is somehow confirmed also by the appearance of the Rayleigh wave fundamental mode, exhibiting phase velocities ≈ 450 m/s between 7-12 Hz, followed by an inflection at 6 Hz and then (<6 Hz) a steep slope towards high velocity values: this pattern is generally associated to a S-wave velocity inversion in the subsurface (Maraschini and Foti, 2010; Bergamo et al. 2011).

In agreement with the Geopsy format for inversion target, all dispersion modes of Figure 17 were finally resampled using 200 points between 0.5 and 100 Hz, uniformly spaced on a logarithmic scale.
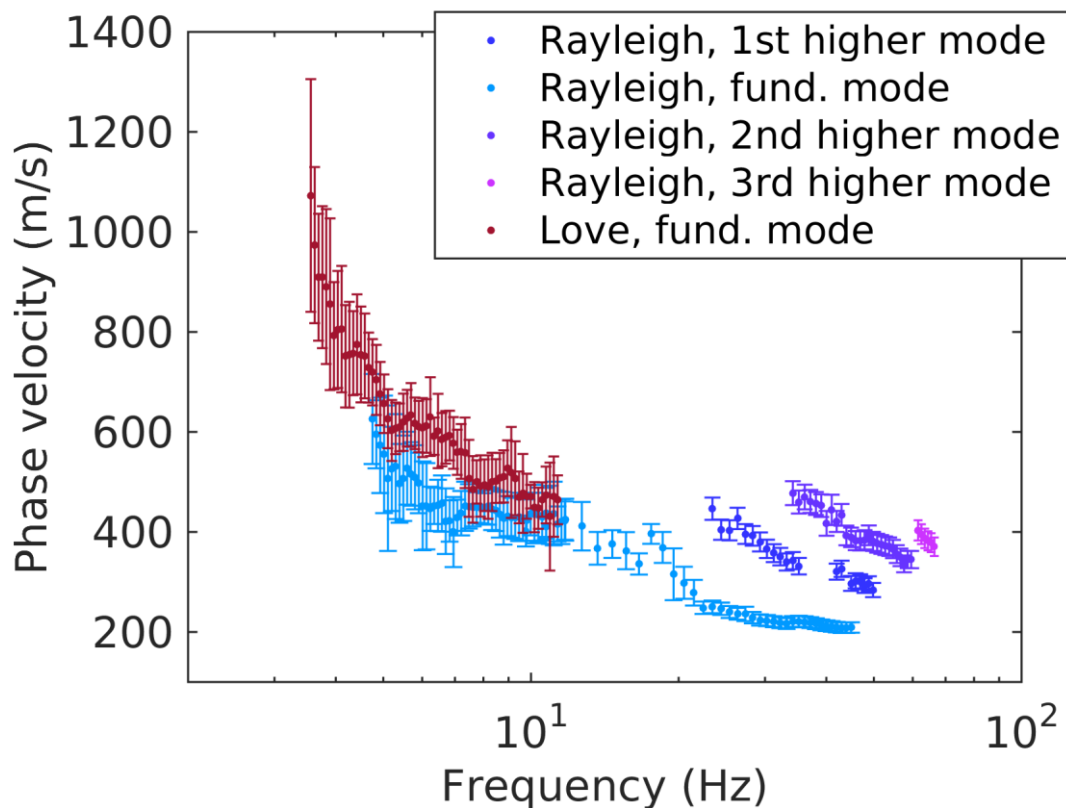
Figure 17 – Inversion target. Rayleigh wave fundamental and 1st-3rd higher modes from active and passive surface wave surveys, and Love wave fundament mode exclusively from passive array data processing.

5.2   Parameterization of the model space

After several preliminary attempts, the subsurface was modeled as 6-layers plus half-space. This relatively high number of layers was made necessary by:

-        The relative complexity of the weathering formations, identified with the P-wave refraction interpretation (section 4.2.1). A three-layer profile, derived from that in Figure 13b (left panel), was

chosen to model the shallow subsurface (0-12 m), as representative for the centre of the active array (which is the location the active data dispersion curve is referred to, also considering the seismogram windowing adopted prior to the application of the f-k transform; see section 4.2.2). For these first three layers, velocity and thickness intervals are relatively narrow and closely follow the reference profile in Figure 13b (left panel); the Poisson ratio interval is 0.2-0.4, which is suitable for unsaturated uncohesive formations;

- the need to model a velocity inversion (i.e. a softer layer embedded within stiffer formations) at intermediate depths (~ 20 m). As discussed in the previous paragraph, this feature is indicated by the shape of the Rayleigh and Love wave fundamental modes at low frequencies. Also, all preliminary inversion attempts forcing an increase of V_S with depth (i.e. not allowing for a velocity inversion) did not succeed in fitting both Rayleigh and Love wave dispersion curves.

As no reliable geological information was available for these deeper formations (layer 4 − 7), both their thicknesses and velocities were left free to vary within broad intervals. The Poisson's ratio range was 0.2 − 0.48 (to allow for the presence of saturated layers), with the exception of the half-space (for which a narrower interval 0.2 − 0.3 was chosen).

5.3   Inversion results

Adopting the parameterization introduced in the previous section, an inversion run involving the test of 500 000 subsurface profiles was performed. The obtained velocity profiles (top panels, in Figure 18) appear to converge towards a rather definite subsoil model, although some variability in the estimation of the parameters of the deeper layers can be observed. This variability can be ascribed to the necessity to model the subsurface with a relatively high number of layers, and to the lack of reliable a priori geological information for the site, which forced us to adopt wide boundaries, particularly for the parameters of the deepest layers. Nevertheless, the equivalence among different solutions is intrinsic to surface wave data inversion (Foti et al., 2009), and should be regarded as an aspect of the epistemic uncertainties of the analysis, rather than as failure to achieve the "true" model. The best performing profiles in Figure 18 (top panel) follow a gradual increase of seismic properties with depth in the surficial layers, until a relatively stiff formation ($V_S \approx 890$ m/s) is met at approximately 13 m depth. Below this layer, the S-wave velocity is substantially slower (370 m/s), then it increases again until the half-space is reached ($V_S \approx 1500 − 2000$ m/s, depth ~ 49 m).

The overall agreement between experimental and simulated curves can be considered as satisfactory (Figure 18, center and bottom panels). Synthetic curves follow the experimental data with a good level of approximation across all the frequency range, both for the multimodal Rayleigh wave dispersion curve and the Love wave fundamental mode.
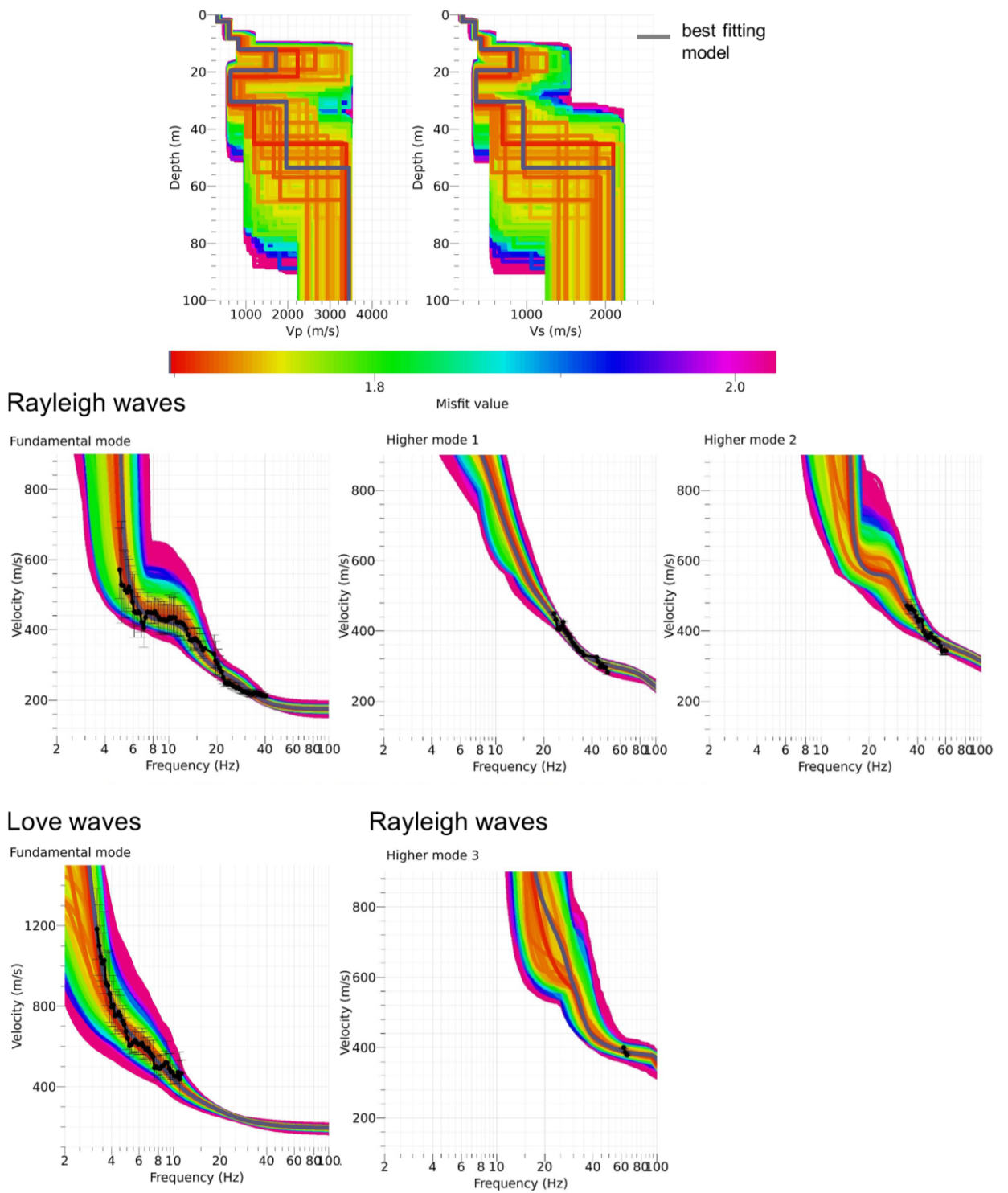
Figure 18 – Inversion results. Top: ground profiles. Centre and bottom: fitting between experimental and synthetic data. The best fitting model is represented with gray lines.

6   Interpretation

In this section, the geological interpretation of the obtained velocity profiles as well as the relevance of 2D resonance phenomena are discussed.

6.1   Interpretation of the velocity profiles

The model achieving the lowest misfit value (RMSE = 1.623) is represented by gray lines in Figure 18. To define a set of "companion" reliable profiles capable of expressing the degree of uncertainty of the inversion estimate, we select an ensemble of models reaching a misfit value close enough to the minimum RMSE, so that these models can be considered statistically equivalent (i.e. equally reliable) to the best performing profile according to a Fisher test with 66.6% confidence interval (Maraschini and Foti, 2010). This model ensemble is constituted by the best fitting profile and 24 additional models (i.e. it is the set of the 25 best performing subsurface models, with RMSE = 1.623-1.682). These profiles are displayed in Figure 19 and they are considered here for the geological interpretation.

As earlier anticipated, the shallow subsurface is modeled as a set of three layers, derived from P-wave refraction interpretation. These layers are characterized by values of V_S increasing with depth (190, 260 and 425 m/s, respectively) and have an overall thickness of 12.5 m. They can be interpreted, from top to bottom, as artificial soil cover, a transition layer, and a layer of debris flow sediments, composed by sand, gravels, and pebbles (following the information of the Swisstopo geological map in Figure 1, and the log from the available borehole closest to SZEK, about 100 NE of SZEK, see Figure 1). Below these surficial formations, a stiffer layer with $V_S \approx 890$ m/s and thickness of ~ 10 m is met. This higher value of S-wave velocity could be explained with a formation of debris flow sediment with a greater fraction of gravels and pebbles. This formation is followed by a 10 m thick layer with S-wave velocity of 370 m/s, probably mostly constituted by sand. The selected V_S profiles, quite consistent in the description of this shallower portion of the subsurface, present a larger variability for the parameters (thickness and velocity) of the two deepest layers. In fact, below the low-velocity layer at depths between 20 and 30 m, a transition formation with velocities ranging between 600 and 1000 m/s is identified; the depth of its lower interface varies between 40 and 70 m, although most of the selected profiles place its lower boundary (which coincides with the bedrock depth) at around 49 m depth (median of the distribution = 48.6 m). We remark that this value is compatible with the logs from the two boreholes closest to SZEK, indicating the depth of the bedrock at 46 and 50 m, respectively (Figure 1). Finally, the half-space S-wave velocity is estimated to be between 1500 and 2100 m/s; these values are suitable for the identification of this layer as the valley bottom bedrock.
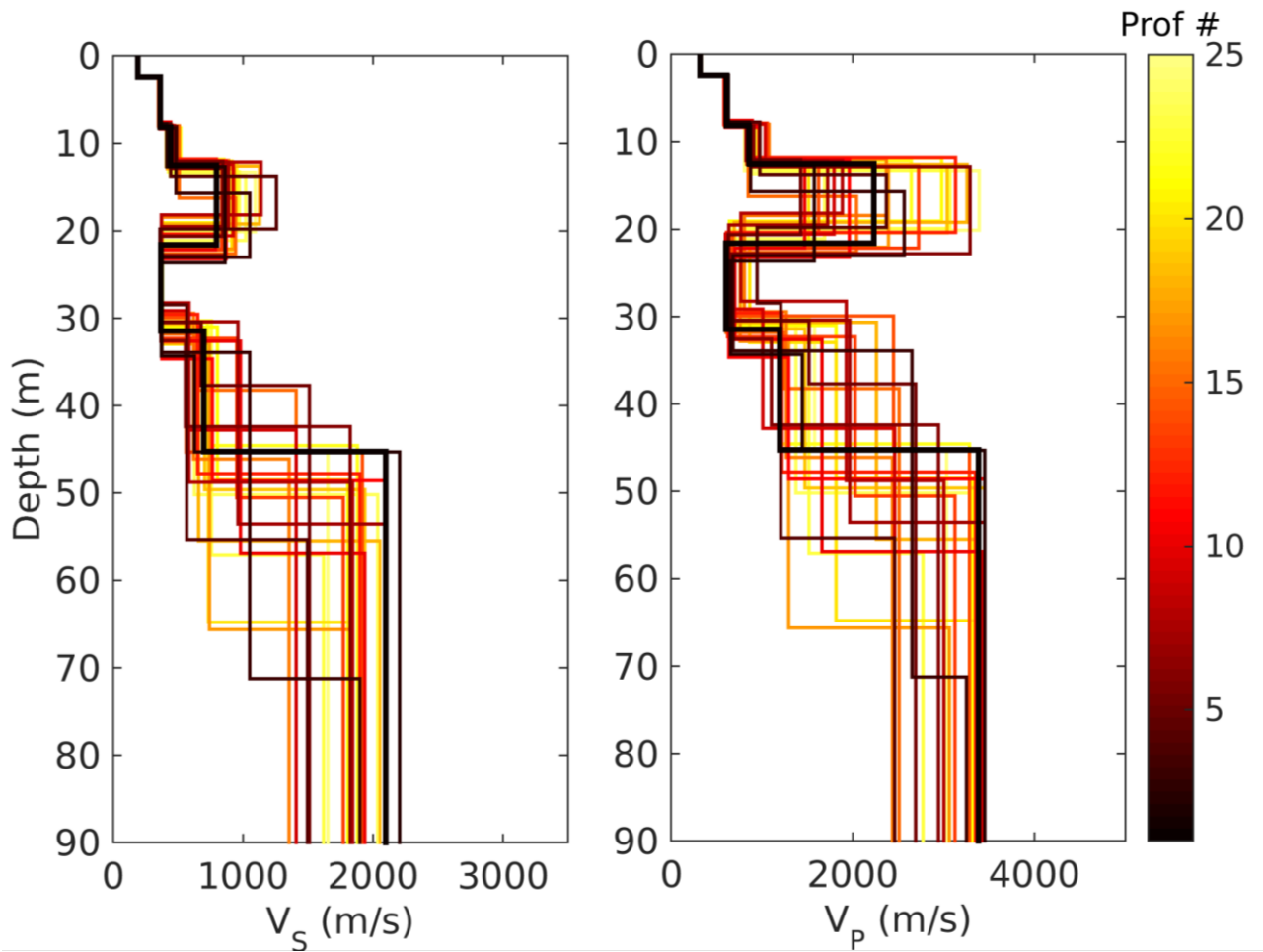
Best performing profiles

Figure 19 – 25 best performing velocity profiles (RMSE < 1.682), considered as statistically equivalent to the best model (RMSE = 1.623) according to a Fisher test with 66.6 % confidence interval. The color scale follows the sorting of the profiles according to RMSE; the best model is therefore represented with a black (and also thicker) line.

6.2   2D Resonance

The geomorphology of the investigated area, i.e. the bottom of an alpine valley, can suggest the presence of a 2D resonance behavior for site SZEK. Nonetheless, the empirical observations do not univocally confirm this condition.

Indeed, the results of the polarization analysis (section 4.1.2) indicate a marked directionality of microtremors in the fundamental peak frequency band (2.5 – 3.5 Hz), oriented along the valley axis. Of course, the valley axis is also a preferential direction of propagation (Figure 11), as human population and its activities are mainly concentrated in the valley bottom. Nevertheless, the polarization observed at 2.5 – 3.5 Hz definitely stands out with respect to lower or higher frequencies (Figures 8 and 9). On the other hand, the fundamental frequency peaks (determined from H/V analysis) display also a spatial variability, proper of 1D resonance condition (section 4.1.1, Figure 7);, the f_0 spatial distribution is compatible with the inferred configuration of the valley bedrock–

sediment interface (fundamental frequencies are higher close to the valley edge, and they become lower and lower as one descends along the main axis of the valley, where a thicker sedimentary cover is to be expected).

In order to add further material for discussion, the compatibility between the shape of the valley at SZEK and critical geomorphologies identified in literature for the onset of 2D resonance phenomena was also investigated.

According to Bard and Bouchon (1985), in sediment-filled valleys 2D resonance prevails over 1D when the valley shape ratio (h/l) exceeds a critical value defined as

$$(h/l)_c = 0.65 \, (C_v-1)^{1/2} \tag{1}$$

where h is the maximum thickness of the sedimentary cover, l is the half-width of the valley (the width at $h/2$ depth) and C_v is the velocity contrast between sediments and bedrock. Unfortunately, we do not have much information regarding the actual shape of the valley sediments at site SZEK. The width of the sedimentary cover (w) was estimated as 442 m observing the topography of the section of the valley and the extension of sedimentary formations from the geological map (Figure 20). As in Bard and Bouchon (1985), a cosine-shaped profile for the valley was assumed. Consequently, the thickness h of the sediments at the valley centre was derived imposing a bedrock depth equal to that of the half-space in Figure 19, at a distance of 100 m from the basin edge (distance of SZEK from the NW valley shoulder, Figure 20); therefore, h ranges between 90 - 165 m. The half-width l of the valley sediments filling was obviously set to 221 m (half of the valley width at the soil surface w), independently of h. The velocity contrast Cv was again determined from the selected models in Figure 19. The obtained couples of shape ratio vs velocity contrast are shown as circles in Figure 21.; they gather within the portion of Cv-h/l graph corresponding to a 2D resonance behavior, although quite close to the critical shape ratio line. A condition of transition between 1D and 2D resonance could therefore explain the co-existence of experimental evidences from both behaviors.
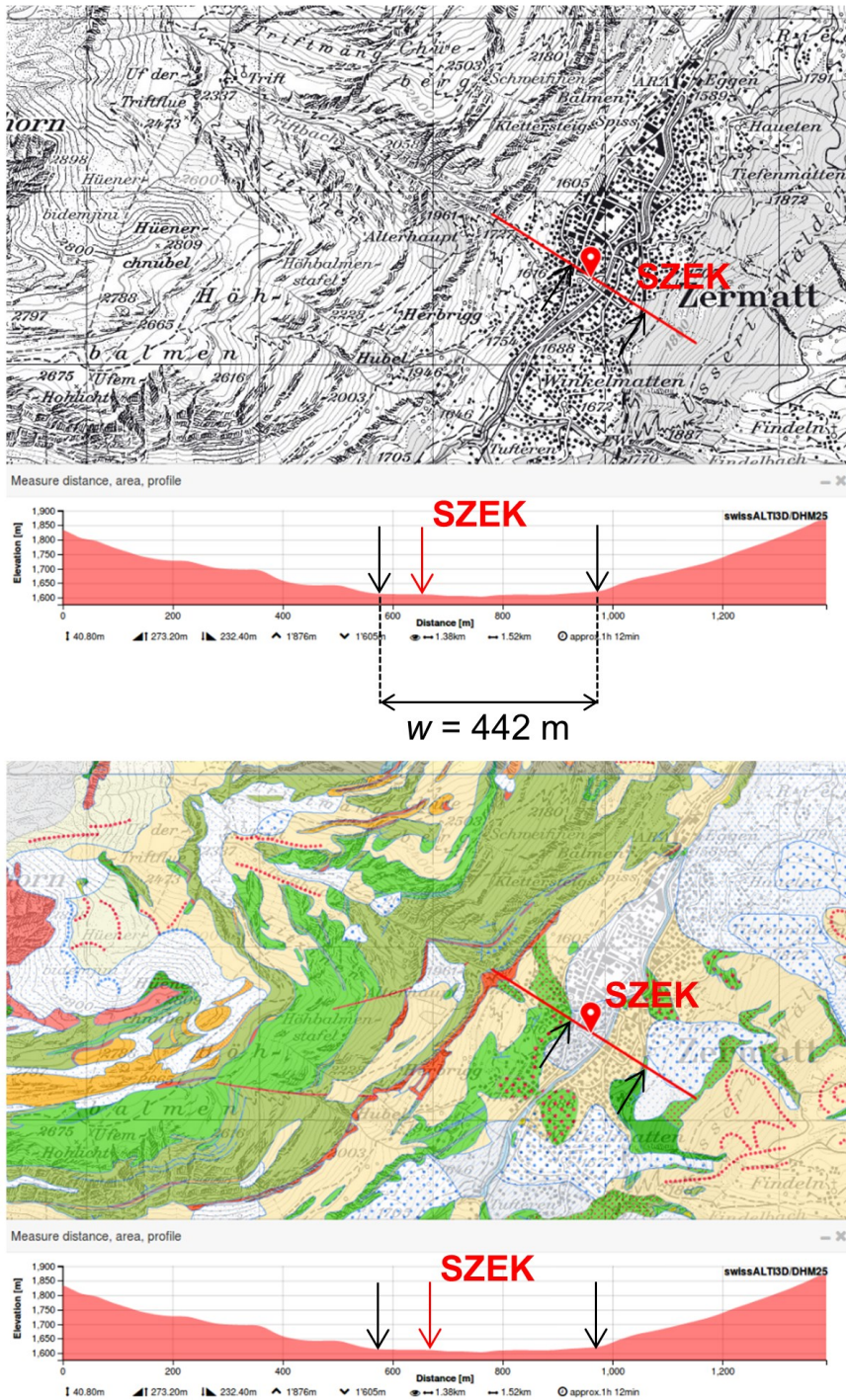
Figure 20 – Geometry of sediments in the Mattertal valley at site SZEK. The surficial width (w) of the sedimentary formations was estimated as 442 m by combining the topography of the valley section (top) with the soil cover map (bottom; (© 2017 Swisstopo, JD100042).
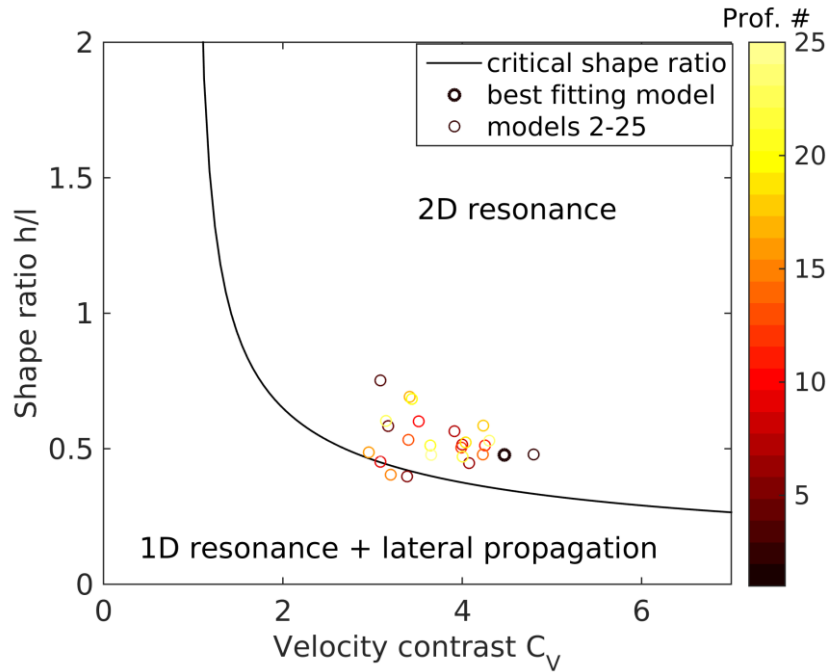
Figure 21 – Shape ratio vs velocity contrast graph (see Bard and Bouchon, 1985). Colored circles represent the h/l-Cv coordinates derived from the velocity profiles in Figure 19 (same color scale), assuming a resonant basin occupying a cosine-shaped valley bottom.

Using the formula of Bard and Bouchon (1985), the resonance frequency of cosine-shaped valley can be obtained as

$$f = \frac{v_S}{4h}\sqrt{1+\left(\frac{4h}{l}\right)^2},$$

(2)

where v_S is the average shear-wave velocity in the basin, h and l the same of equation 1). With this formula and the values obtained from the inverted profiles ($v_S ==440 - 615$ m/s) and from the geometry supposed in the previous case ($h = 90 – 165$ m, $l = 221$ m) we derive a set of feasible resonance frequencies for the valley basin whose distribution partly overlaps that of the f_0 values determined from H/V analysis (Figure 22). On average, however, the latter have a mean value (3.03 Hz) larger than that of the results of equation 2 (2.45 Hz).

It is worth remarking that the application of equations 1 and 2 presupposes a homogeneous sedimentary filling inside a bedrock of a defined geometry (cosine-shaped valley). This modeling might be too simplistic to explain the real case of Zermatt; in fact, the sedimentary cover of the Matttertal in Zermatt is not homogeneous (it is partly moraine, partly alluvial deposits), and we do not have any information regarding the actual profile of the bedrock-sediments interface.

To conclude, a state of transition between 1D and 2D resonance appears to be the most plausible condition for SZEK.
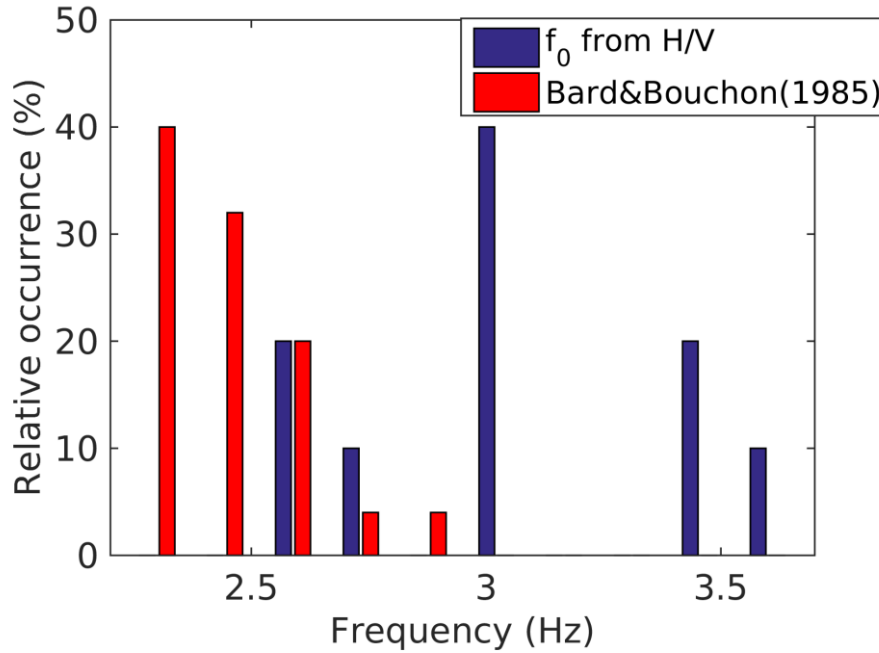
Figure 22 – Comparison between the distribution of resonance frequencies obtained from the profiles of Figure 20 and equation 2 (Bard and Bouchon, 1985, red histogram), and of frequencies of peaks from H/V analysis (section 4.1.1, blue histogram).

6.3   Quarter-wavelength representation

In Figure 23 we show the quarter-wavelength representation (Joyner et al., 1981) in terms of depth (top panel), velocity (centre) and impedance contrast (bottom), averaged over the selected final profiles of Figure 19.

The quarter-wavelength depth (top panel), in particular, is considered a useful proxy in estimating the depth of reliable investigation of the available experimental data. In the presented case, the minimum frequency of the inverted phase velocity data is 3 Hz (Love wave fundamental mode), which corresponds to a quarter-wavelength depth of 37 m (Figure 23, top panel).

The quarter-wavelength velocity at the frequency of the quarter-wavelength depth of 30 m corresponds to a V_{S30} value of 414 m/s.
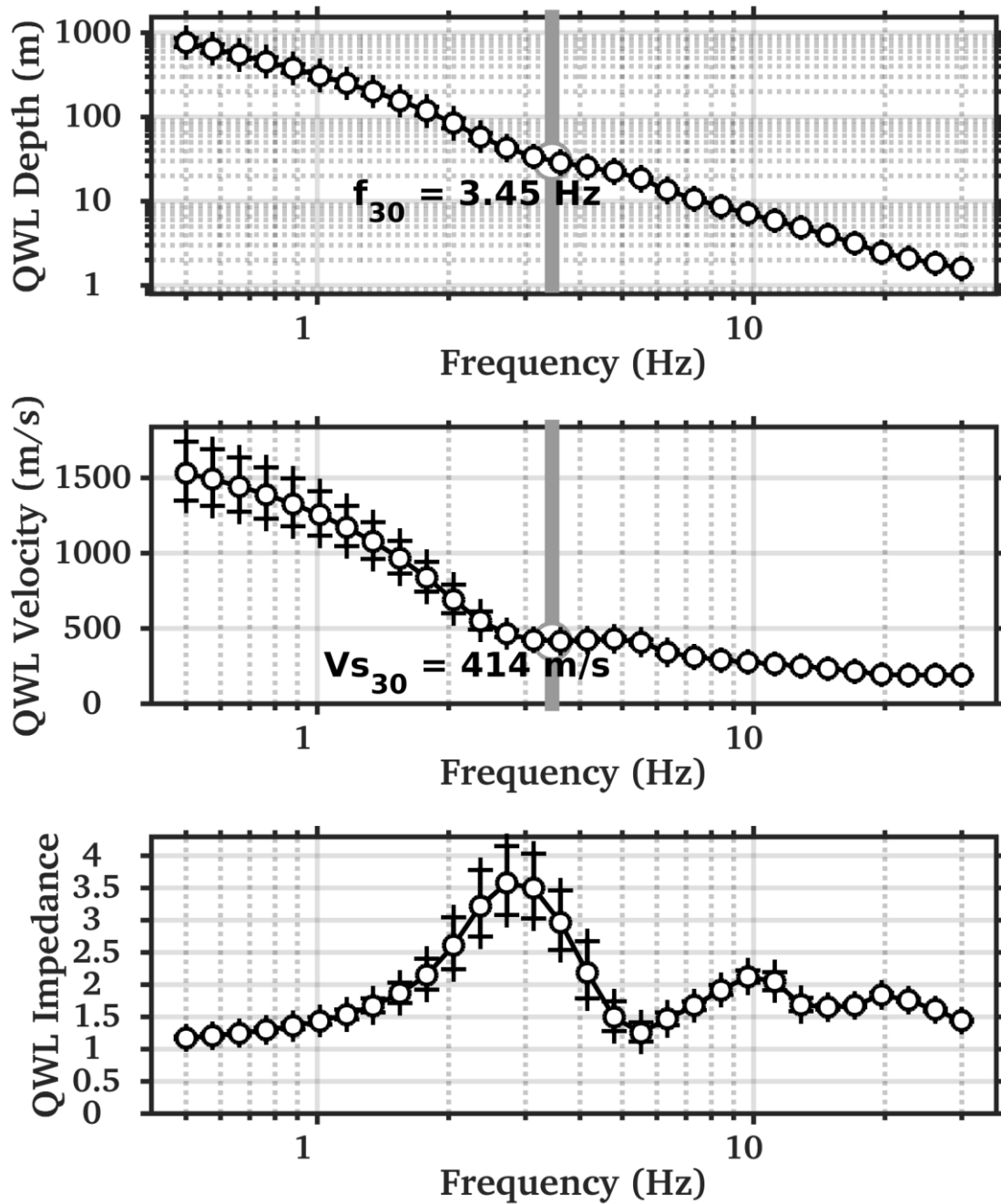
Figure 23 – Average quarter-wavelength (qwl) representations for the final profiles displayed in Figure 19. Top: qwl-depth; center: qwl-velocity; bottom: qwl-impedance contrast. The gray line in the top and center panel refers to Vs₃₀.

6.4   SH transfer function

The theoretical SH-wave transfer functions for vertical propagation (Roesset, 1970) were computed for the selected models (profiles in Figure 19), and corrected for the Swiss reference rock model (Poggi et al., 2011).

In Figure 24, these functions are compared with the amplification function obtained by empirical spectral modeling (ESM; Edwards et al., 2013; Michel et al., 2014). Both the simulated and the empirical transfer functions agree in identifying the fundamental frequency at around 2.7 Hz. It should be noted, however, that due to the possible 2D resonance effects (section 4.1.2), we would expect the f_0 peak of the synthetic transfer functions, computed with a 1D assumption, to be slightly smaller than the one from the empirical function. This can be partly explained with the fact that SZEK is probably at the threshold between 1D and 2D resonance conditions, as proposed in 6.2.

Above the fundamental peak at 2.7 Hz, and until 14 Hz, the empirical amplification function presents a frequency band with approximately constant amplification value; this feature is generally associated with edge-generated surface waves (Michel et al., 2014), that arise at the borders of sedimentary basins due to the interaction between body waves and the wedge-shaped sediment boundaries (bordered at the top by the flat soil surface and at the bottom by the sloping interface sediments/bedrock). Indeed, the geomorphology of SZEK is compatible with the presence of such phenomenon. The synthetic SH transfer functions in Figure 24, computed with a 1D model assumption, are obviously unable to reproduce this frequency band with constant amplification; instead, they present a second peak at 10 Hz, which is related to the impedance contrast at the upper interface of the stiff layer at 12.5 m depth (Figure 19). Interestingly, a peak at around 10 Hz can be found in some H/V graphs from passive array sensors recordings (Figure 6).

Finally, it is worth pointing out that, despite the relative variability among the V_S profiles resulting from the inversion (Figure 19), these yield similar SH transfer functions (colored lines in Figure 24). In fact, as observed for instance by Foti et al. (2009), V_S models that are equivalent from the point of view of surface-wave testing, are also equivalent with respect to site amplification.
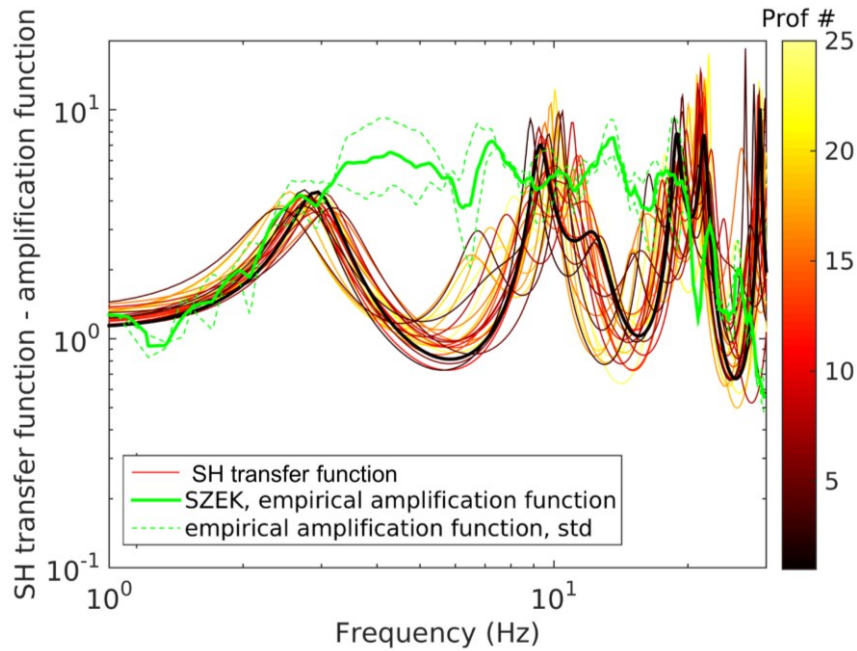
Figure 24 – Modeled SH transfer function (red to yellow lines) from the selected velocity profiles (Figure 19), corrected for the Swiss reference rock model. In green, the amplification function obtained by spectral modeling.

7 Conclusions

Active and passive seismic surveys were performed to characterize the structure of the subsurface below the SSMNet station SZEK, located in the centre of Zermatt, Canton Valais. Passive data were processed to derive Rayleigh and Love wave dispersion curves; active data were analyzed to estimate the high-frequency portion of the Rayleigh wave dispersion curve, and to obtain a V_P model for the shallow subsoil from P-wave refraction.

The polarization analysis of the passive recordings evidenced a strong directionality (along the valley axis) at the frequencies close to f_0 (2.5-3.5 Hz). This behavior was ascribed to a condition at the threshold between 1D and 2D resonance for the sedimentary formation on top of which station SZEK was installed. The empirical amplification function of SZEK suggests also the presence of edge-generated surface-waves as site amplification effect.

The velocity profile derived from the surface wave data inversion process is characterized by a gradual increase of V_S at shallow depths (until 12.5 m, from V_S = 190 m/s at the surface to 460 m/s), related to sandy/gravelly sediments with increasing degree of compaction. Below (12.5 – 22.5 m depth), a stiffer layer with S-wave velocity of 890 m/s is met, probably characterized by a significant fraction of stones and pebbles. Between 22.5 and 32.5 m depth, the identified Vs is lower (370 m/s), possibly corresponding to a purely sandy layer. At greater depths, the Vs profiles show a larger variability in the estimation of the subsoil parameters; a transition layer (V_S = 600 – 1000 m/s) interposes between the upper soft formation and the bedrock below (V_S = 1500 – 2000 m/s, composed of ophiolite). The obtained depths for the sediment-bedrock boundary range within 30 – 70 m, although their distribution concentrates around the median value of 48.6 m. Nearby boreholes present similar values (46-50 m).

The obtained V_{S30} is 414 m/s, thus classifying the soil as type B according to Eurocode 8 (CEN, 2004), and as type C following SIA261 (SIA, 2014).

References

Bard, P.-Y., and M. Bouchon, 1985. The two-dimensional resonance of sediment-filled valleys, Bull. Seismol. Soc. Am. 75, no. 2, 519–541.

Bergamo, P., C. Comina, S. Foti and M. Maraschini, 2011. Seismic characterization of shallow bedrock sites with multimodal Monte Carlo inversion of surface wave data. SDEE, 31, no.3, 530-534.

Bergamo, P., A. Darzi, and D. Fäh, 2016. Site characterization report, SBIK – Biel Kongresshaus. SED report.

Boiero, D., 2009, Surface wave analysis for building shear wave velocity models: Ph.D. thesis, Politecnico di Torino

Boiero, D., and L. V. Socco, 2010, Retrieving lateral variations from surface wave dispersion curves analysis: Geophysical Prospecting, **58**, 977–996

Burjánek J., G. Gassner-Stamm, V.Poggi, J. R. Moore, and D. Fäh, 2010. Ambient vibration analysis of an unstable mountain slope. Geophysical Journal International, 180(2):820–828, February 2010. ISSN 0956540X.

CEN, 2004. Eurocode 8: Design of structures for earthquake resistance – Part 1: general rules, seismic actions and rules for buildings. European Committee for Standardization, en 1998-1 edition.

Edwards, B., Michel, C., Poggi, V., and Fäh, D. , 2013. Determination of Site Amplification from Regional Seismicity : Application to the Swiss National Seismic Networks. Seismological Research Letters, 84(4).

Fäh, D., F. Kind, and D. Giardini, 2001. A theoretical investigation of average H/V ratios. GJI, 145, no. 2, 535-549.

Géoportail du Canton Valais, 2017. *https://geocadast.crealp.ch/index.php?mode=display&view=carte.* Accessed 20/03/2017.

Geopsy, 2017. *http://www.geopsy.org/.* Accessed 20/03/2017.

Foti S., C. Comina, D. Boiero, and L.V. Socco, 2009. Non-uniqueness in surface-wave inversion and consequences on seismic site response analysis. Soil Dynamics and Earthquake Engineering, 29, 982-993.

Foti, S., Lai C.G., Rix G.J., and C. Strobbia, 2015, Surface Wave Methods for Near-Surface Site Characterization: CRC Press, Taylor & Francis Group LLC

Hobiger, M., C. Cornou, M. Wathelet, G. Di Giulio, B. Knapmeyer-Endrun, F. Renalier, P.Y. Bard, A. Savvaidis, S. Hailemikael, N. Le Bihan, M. Ohrnberger, and N. Theodoulidis, 2013. Ground structure imaging by inversion of Rayleigh Rayleigh wave ellipticity: sensitivity analysis and application to European strong motion sites. GJI, 192, 207-229.

Joyner, W. B., Warrick, R. E., and Fumal, T. E., 1981. The effect of Quaternary alluvium on strong ground motion in the Coyote Lake, California, earthquake of 1979. Bulletin of the Seismological Society of America, 71(4):1333–1349.

Maranò S., 2016. http://mercalli.ethz.ch/~marra/WaveDec/userguide_WaveDec.html

Maranò, S., M. Hobiger, P. Bergamo and D. Fäh, 2017. Analysis of Rayleigh Waves with Circular Wavefront: a Maximum Likelihood Approach. GJI, 210 (3), 1570-1580.

Maraschini M., and S. Foti, 2010. A Monte Carlo multimodal inversion of surface waves. GJI, 182 (3). 1557 – 1566.

Michel, C., B. Edwards, V. Poggi., J. Burjanek, D. Roten, C. Cauzzi, and D. Faeh, 2014. Assessment of Site Effects in Alpine Regions through Systematic Site Characterization of Seismic Stations. BSSA, 104, no. 6, 2809-2826

Neducza, B., 2007, Stacking of surface waves: Geophysics, 72, 51–58.

O'Neill, A., 2003, Full-waveform reflectivity for modelling, inversion and appraisal of seismic surface wave dispersion in shallow site investigations: PhD thesis, University of Western Australia, Perth, Australia.

Park, C. B., R. D. Miller, and J. Xia, 1999. Multichannel analysis of surface waves: Geophysics, **64**, 800–808.

Poggi, V., Edwards, B., and Fäh, D. (2011). Derivation of a Reference Shear-Wave Velocity Model from Empirical Site Amplification. Bulletin of the Seismological Society of America, 101(1):258–274.

Poggi, V., and D. Fäh, 2009. Estimating Rayleigh wave particle motion from three component array analysis of ambient vibrations. GJI, 180, no. 1, 251-267.

Redpath, B. B., 1973, Seismic refraction exploration for engineering site investigations: National Technical Information Service, Technical Report E-73-4.

Reynolds, J.M., 2011, An introduction to applied and Environmental Geophysics: John Wiley & Sons, Ltd.

Roesset, J. (1970). Fundamentals of soil amplification. In Hansen, R. J., editor, Seismic Design for Nuclear Power Plants, pages 183–244. M.I.T. Press, Cambridge, Mass.

SIA, 2014. SIA 261 Einwirkungen auf Tragwerke. Société Suisse des ingénieurs at des architectes, Zurich, Switzerland.

Socco, L.V., D. Boiero, S. Foti, and R. Wisen, 2009, Laterally constrained inversion of ground roll from seismic reflection records: Geophysics, **74**, no. 6, G35-G45.

Socco, L.V., and C. Strobbia, 2004, Surface-wave method for near-surface characterization: a tutorial: Near Surface Geophysics, **2**, no. 4, 165-185.

Swisstopo, 2017. Atlas géologique de la Suisse, 1:25000, Feuille 29.

Wathelet, M., 2008. An improved neighborhood algorithm: Parameter conditions and dynamic scaling. GRL, 35, no.9, 1-5.